This is a preprint, the final version is subject to change, of the American Mineralogist (MSA)
Cite as Authors (Year) Title. American Mineralogist, in press.
(DOI will not work until issue is live.) DOI: http://dx.doi.org/10.2138/am.2014.4353

Revision 1

Diffusion of Helium in Natural Monazite, and Preliminary Results on He diffusion in Synthetic Light Rare Earth Phosphates

D.J. Cherniak, E.B. Watson
Department of Earth and Environmental Sciences
Rensselaer Polytechnic Institute
Troy, NY 12180 USA

Abstract

Diffusion of helium has been characterized in natural monazite and synthetic LREE phosphates. Polished slabs of natural monazite and flat growth faces of synthetic phosphates were implanted with 100 keV ^{3}He at a dose of $5x10^{15}$ ^{3}He/cm^2 and annealed in 1-atm furnaces. ^{3}He distributions following experiments were measured with Nuclear Reaction Analysis using the reaction ^{3}He(d,p)^{4}He. For diffusion in monazite we obtain the following Arrhenius relation for diffusion normal to (100):

$D = 1.60x10^{-7} \exp(-150 \pm 8 \text{ kJ mol}^{-1}/RT)$ m^{2}sec^{-1}.

Diffusion in natural monazite exhibits little diffusional anisotropy, as diffusion normal to (001), (100) and (010) appear similar, as do diffusivities of He in natural monazites from two different localities. Over the investigated temperature range, these diffusivities are similar to those of Farley and Stockli (2002), and values obtained for some of the monazite grains analyzed by Boyce et al. (2005), obtained through bulk-release bulk release of He by step heating, and are bracketed by diffusivities obtained by Farley (2007) for monazite-structure synthetic REE phosphates.

He diffusion measured in synthetic REE phosphates ($LaPO_4$, $NdPO_4$, $SmPO_4$ and $EuPO_4$) with the monazite structure appears to behave systematically, with diffusion in the lighter REE phosphates slightly faster than in the heavier REE phosphates. This trend is in broad agreement

with the findings of Farley (2007), but the difference in diffusivities among the REE phosphates is smaller than that reported by Farley (2007). Activation energies for He diffusion in the synthetic LREE phosphates are similar to that for natural monazite measured in this study, but He diffusivities in synthetic $LaPO_4$ are about an order of magnitude faster than in the natural monazites.

The differences in He diffusivities among the natural monazites and synthetic REE phosphates may be a consequence of the density and distribution of interstitial apertures in the crystal structure, which may result in differences in He migration rates. The similarities in He diffusivities for natural monazites containing varying mixtures of rare-earth elements, as well as differences in Th contents, however, indicate that the above Arrhenius relation is most relevant for describing He diffusion in monazite in nature.

We use this Arrhenius relation to evaluate He retentivity in monazite experiencing thermal events, using both Dodson's (1973) closure temperature formulation and recently developed expressions (Watson and Cherniak, 2013) for prograde thermal events and heating and cooling trajectories. Calculations indicate that monazite is comparatively retentive of He among accessory mineral phases.

Keywords: monazite, xenotime, rare-earth orthophosphates, helium, diffusion, nuclear reaction analysis, thermochronology

1. Introduction

The relatively rapid diffusion rates and consequently low closure temperatures of He allow insights into the time-temperature evolution of rocks that would be inaccessible by other means. (U-Th)/He ages for apatite, zircon, titanite, rutile, and monazite, when coupled with a quantitative understanding of the effects of temperature on measured ages due to diffusional loss and conditions for He retention in minerals, can be used to map thermal structure to estimate the timing, rate, and structural details of the process of exhumation and various near-surface tectonic and geomorphic processes (e.g., Wolf et al., 1996; 1998; House et al., 1997;1998; Reiners et al., 2000; Reiners and Farley, 2001; Farley, 2002; Farley and Stockli, 2002; Ehlers and Farley, 2003; Reiners et al., 2005; Stockli, 2005; Shuster and Farley, 2005a). With advancement of analytical techniques, these methods have found greater application (e.g., Farley, 2002; 2000; Reiners et al, 2002; 2004; 2005; Wolf et al., 1998; Shuster et al., 2006; Shuster and Farley, 2009). Further understanding of He diffusion kinetics is essential for evaluating conditions under which He is lost or retained in specific minerals and in refining interpretations of time-temperature histories.

Much of the present knowledge of the diffusion behavior of monazite and other REE orthophosphates has been obtained through outgassing studies, where samples are heated in a stepwise manner and the He released is measured by mass spectrometery (e.g., Farley, 2007; Boyce et al., 2005; Farley and Stockli, 2002). While the employment of these methods has provided invaluable information about the He diffusion systematics of many mineral phases, several limitations exist. The “bulk release” patterns obtained in these studies do not provide information about initial distributions of helium. Helium may be nonuniformly distributed, depending on the distribution of U and Th in mineral grains, alpha ejection from mineral grains during radioactive decay, and differential He losses due to past thermal histories. In addition,

77 microstructures within mineral grains may create diffusion fast paths, which cannot be readily
78 distinguished from lattice diffusion because profiles are not measured directly in these analyses.
79 Refinements of step-release techniques (e.g., Shuster and Farley, 2004; 2005a,b; Shuster et al.,
80 2004) which involve the generation of a uniform ^{3}He distribution by proton irradiation, coupled
81 with measurement of the ratio of simultaneously released ^{4}He/^{3}He, have helped to surmount
82 some of these difficulties and provide more detailed information about the ^{4}He distributions
83 within mineral grains. However, non-Arrhenian and other poorly understood diffusion behaviors
84 have been observed for helium in some step-heating studies.
85 Direct profiling to characterize diffusion of implanted ^{3}He and ^{4}He in phosphates, oxides
86 and silicates has been undertaken using the techniques of nuclear reaction analysis (NRA) and
87 Elastic Recoil Detection (ERD) (e.g, Ouchani et al., 1998; Miro et al. 2007; 2006; Trocellier et
88 al., 2003a,b; Gosset et al., 2002; Constantini et al., 2002; Cherniak et al., 2009; Cherniak and
89 Watson, 2011; 2012a), and LA-ICPMS (Hodges et al., 2009; van Soest et al., 2011). These
90 studies complement the findings from bulk release experiments and provide additional
91 constraints on He diffusion. In previous work, we have presented results for He diffusion in
92 zircon and apatite (Cherniak et al., 2009), and titanite and rutile (Cherniak and Watson, 2011). In
93 the present study, we continue work on measurements of He diffusion in accessory minerals with
94 a study of natural monazite and synthetic REE phosphates with the monazite structure, taking a
95 similar approach to that in these earlier studies, where ion implantation was used to introduce
96 ^{3}He, and ^{3}He concentrations were measured by nuclear reaction analysis.
97 Anisotropy of helium diffusion may be pronounced in some mineral phases, as has been
98 observed recently in measurements of zircon (Cherniak et al., 2009; Hodges et al., 2009) and
99 rutile (Cherniak and Watson, 2011). Since the existence and extent of anisotropy may be difficult

to evaluate through bulk-release techniques, direct profiling of He distributions to evaluate diffusion coefficients may provide additional understanding of diffusion behavior and processes. These methods offer a means to directly profile He distributions, permitting direct determinations of diffusional anisotropy. NRA depth profiling measurements, in this case using a deuterium beam to induce nuclear reactions with ^{3}He introduced into the sample by ion implantation, probe the outer few μm of oriented samples, yielding essentially 1-dimensional geometry in analysis, in contrast to bulk-degassing experiments, where He is released and detected simultaneously from all sides of the sample. NRA also permits direct profiling of much shorter profiles than laser ablation depth profiling (e.g., van Soest et al., 2011), so diffusivities at lower temperatures, which may be closer to those of geological relevance, can be measured. Ion implantation is a means to introduce He in a controlled dose and distribution (determined by the implanted ion energy and the material) in the sample, so there are no analytical artifacts due to initial zoning or other intragrain variations of He concentrations in mineral samples. Such variations may be a significant factor in monazite, where zoning in Th is frequently observed (e.g., Pyle et al., 2001, Kohn and Malloy, 2004; Yang and Pattison, 2006), which could result in nonuniform distributions of ^{4}He within a mineral grain. Further, studies of He diffusion in natural monazite by Boyce et al. (2005) suggest that intergrain variations in He diffusivities may be due to compositional variations, possibly substitutions of Y and Th for Ce, and/or a consequence of potential influences on He release patterns due to internal zoning of U and Th in individual grains. Among synthetic REE phosphates of the monazite structure, Farley (2007) observed that He diffusivities vary with monazite composition, with faster diffusivities for the lighter REE phosphates than for heavier REE phosphates. To explore some of these potential compositional effects, we performed experiments on natural monazites from two different

localities, with differing Th contents, and on four synthetic REE phosphates ($SmPO_4$, $LaPO_4$, $NdPO_4$, and $EuPO_4$).

2. Experimental Procedure

2.1 Sample Preparation

The natural monazites used in the experiments were specimens from Brazil and North Carolina. Samples from the latter locality have been used in previous studies of Pb (Cherniak et al., 2004a) and oxygen (Cherniak et al., 2004b) diffusion. These natural monazites were chosen for study because fairly large crystals could be obtained to produce samples with homogeneous regions free of cracks and inclusions of sufficient size for analysis. Compositional information on the monazites is in Table 1. While the monazites have similar REE contents, they differ widely in Th concentration, which has the potential to affect diffusivities both through effects on lattice parameters due to altervalent substitutions and differences in degree of radiation damage. Specimens of oriented monazite (to measure diffusion normal to (001) and (100), and (100) and (010) faces in the North Carolina and Brazil monazites, respectively) cut into slabs about 0.5 mm thick and polished to 0.3 μm alumina, followed by a chemical polish with colloidal silica. After polishing, monazite samples were cleaned ultrasonically in distilled water and ethanol. Experiments were also run on synthetic REE phosphates produced by a flux growth method using Na_2CO_3-MoO_3 fluxes (Cherniak et al., 2004c). Each synthetic phosphate contained a single REE (Sm, La, Nd, or Eu); information about these materials (electron microprobe analyses and XRD measurements) is presented in Cherniak et al. (2004c). For the synthetic phosphates, samples with large clean growth faces ((100)) were selected; these received no treatment prior to ion implantation other than ultrasonic cleaning in distilled water and ethanol to remove any residual flux clinging to crystal surfaces.

149
150 **2.2 Ion implantation and diffusion experiments**

151 The synthetic and natural monazite samples (typically sections ~2 to 3mm on a side and
152 0.5-1 mm thick) were mounted for ion implantation on an aluminum plate using carbon paint.
153 The samples were implanted at room temperature with 100 keV ^{3}He ions produced in the Extrion
154 ion implanter at the Ion Beam Laboratory. Doses were $5x10^{15}$ ^{3}He/cm^2. All of the samples to be
155 implanted were mounted together on the aluminum plate and implanted simultaneously, so they
156 received the same implant dose. For the diffusion experiments, implanted specimens were heated
157 in crimped Pt capsules placed in 1 atmosphere Kanthal-wire wound vertical tube furnaces.
158 Experiments were run in air at temperatures from 300-600°C, for times from 20 minutes to 6
159 weeks (Tables 2 and 3). Temperatures in furnaces were monitored with chromel-alumel (type K)
160 thermocouples, with temperature uncertainties ~±2°C. Samples were positioned to within 5mm
161 of thermocouple junctions; hotspots in furnaces used for diffusion anneals were typically about 2
162 cm in length.

163
164 **2.3 NRA measurements**

165 ^{3}He distributions in the samples were measured with Nuclear Reaction Analysis using the
166 ^{3}He(d,p)^{4}He reaction (e.g., Pronko and Pronko, 1974; Dieumegard et al., 1979; Payne et al.,
167 1989; Paszti, 1992). Analyses were performed at the 4 MeV Dynamitron accelerator at the
168 University at Albany. This nuclear reaction has been used to measure ^{3}He in a variety of
169 minerals and ceramic materials, including apatite (e.g., Miro et al., 2006; Cherniak et al., 2009),
170 zircon (Cherniak et al., 2009), zirconia (Gosset et al., 2002, Costantini et al., 2003; Trocellier et
171 al., 2003a,b), britholite (Gosset and Trocellier, 2005; Gosset et al., 2002, Costantini et al., 2002;
172 Trocellier et al., 2003a; b), titanite (Cherniak and Watson, 2011), rutile (Cherniak and Watson,

2011), olivine (Cherniak and Watson, 2012a) and garnet (Roselieb et al., 2006). The protons produced in the reaction, along with backscattered deuterons and products of various (d,p) and (d,α) reactions induced with light elements contained in the sample, were detected with a solid state surface barrier detector with 1500 μm depletion depth and 100 mm^2 area positioned at 167.5° with respect to the incident beam. The beamspot incident on sample surfaces was ~1 to 1.5mm on a side. A 7.5 μm thick Kapton foil was placed in front of the detector to stop some of the backscattered deuterons. Because the protons produced in the $^3He(d,p)^4He$ reaction are so energetic, they stand apart from other contributions to the spectrum, with very little background. The cross-section of the reaction has a maximum around 430 keV, but the peak is relatively broad (several hundred keV in width) so it is not possible to obtain high depth resolution for ^3He profiling using typical approaches for resonant or non-resonant NRA. For these analyses, we take the approach used in earlier studies (Cherniak et al., 2009; Cherniak and Watson, 2011; 2012a), performing analyses over a range of energies (0.5 to 0.9 MeV in this work) to better define the profile, and comparing the proton yield from the annealed sample (i.e., a sample from a diffusion experiment) to an implanted, unannealed sample at each energy step. It should be emphasized that the sampling depth in the monazites in these analyses is up to several microns, considering the ranges for deuterons of these incident energies in monazite (e.g., Ziegler and Biersack, 2006). Given these depth ranges, and that the implanted He will diffuse both toward and *away from* the sample surface, the depth of material interrogated is well in excess of the few hundred nm depth of the implanted He, in contrast to inaccurate statements made (Ketcham et al., 2013) in reference to an earlier study using this method (Cherniak et al., 2009).

These measured ratios were converted into diffusivities by first evaluating the fractional loss of diffusant from an implanted profile as a function of Dt. For a semi-infinite medium with the

concentration of diffusant equal to zero at x = 0, the distribution of the implanted species can be described as a function of depth x and time t as (Ryssel and Ruge, 1986):

$$N(x,t)=\frac{N_m/2}{\sqrt{\left(1+\frac{2Dt}{\Delta R^2}\right)}}\left(\exp\left[-\frac{(x-R)^2}{2\Delta R^2+4Dt}\right]\times\left[1+erf\left(\frac{\frac{R\sqrt{4Dt}}{\sqrt{2}\Delta R}+\frac{x\sqrt{2}\Delta R}{\sqrt{4Dt}}}{\sqrt{2\Delta R^2+4Dt}}\right)\right]+\exp\left[-\frac{(x+R)^2}{2\Delta R^2+4Dt}\right]\times\left[1+erf\left(\frac{\frac{R\sqrt{4Dt}}{\sqrt{2}\Delta R}-\frac{x\sqrt{2}\Delta R}{\sqrt{4Dt}}}{\sqrt{2\Delta R^2+4Dt}}\right)\right]\right) \quad (1)$$

where D is the diffusion coefficient, N_m is the maximum concentration of the implanted species (in an unannealed sample), R is the range (depth in the material) of implanted species, and ΔR is the range straggle (full width at half-maximum width of the initial implanted distribution). Values of R and ΔR for ^{3}He from the Monte-Carlo simulation program SRIM 2006 (Ziegler and Biersack, 2006) are 3520 and 860 Å in the natural monazites; values for N_m are ~0.32 at% for the implanted dose of $5x10^{15}/cm^2$ for the100 keV ^{3}He. For the end-member REE phosphates, values for R and ΔR, respectively, are 3560 and 860 Å for $LaPO_4$, 3550 and 880 Å for $NdPO_4$, 3520 and 880 Å for $SmPO_4$, and 3550 and 900 Å for $EuPO_4$

Equation (1) describes the ^{3}He distribution, but the proton yield measured will be a function not only of the ^{3}He concentration but also of the depth in the material over which the incident deuteron beam can induce the nuclear reaction, the cross-section of the reaction as a function of energy (and depth in the material), the number of deuterons impinging on the target (N_d), and the solid angle subtended by the detector (Ω). The number of detected protons for a profile analyzed with a given beam energy E_o can be determined from the expression

$$N_p(E_0)=N_d(E_0)\Omega\int_{x=0}^{\infty}\frac{d\sigma(E_d(x))}{d\Omega}\rho(x)dx \quad (2)$$

where $d\sigma(E_d(x))/d\Omega$ is the differential cross section for the ^{3}He(d,p)^{4}He reaction at energy E_d, which describes the probability of the reaction occurring at this deuteron energy. The deuteron

energy $E_d(x)$ will be attained at some specific depth x in the material, which is dependent on the incident deuteron energy (E_o) and the rate of energy loss for the deuterons with depth within the material. In the integral above, $\rho(x)$ represents the depth distribution of the diffusant. The above integral is evaluated numerically for each incident deuteron energy by calculating the variation of the reaction cross section with depth in the material. Since the reaction cross section is dependent on deuteron energy, it will vary with depth as energy is lost by incident deuterons traveling through the sample. Values of cross section as a function of energy are derived from the data of Möller and Bensenbacher (1980) and Mayer et al. (2005) corrected for beam-detector angle. These cross-section values are then related to depth in the sample by calculating the energy loss with depth for the incident deuterons for monazite targets using stopping powers obtained from the software SRIM 2006 (Ziegler and Biersack, 2006). The cross-section curves as a function of energy are then used to determine the proton yield from the ^{3}He concentrations $\rho(x)$ across the profile as a function of depth. The values obtained are summed to determine the proton yield for the entire profile for each incident proton energy E_o. The yields for an unannealed implanted reference samples can also be determined in this manner, and a relationship can be determined for each incident beam energy directly relating the ratio of proton yields for an implanted untreated sample and an annealed sample to a specific value of Dt, as outlined in previous work (Cherniak and Watson, 2011; 2012). Uncertainties in diffusivities are determined from counting statistics from the detected proton signals and the variance of calculated diffusivities among incident beam energies used for each sample, which also take into consideration the uncertainties associated with stopping powers in monazite for the incident deuterons and the implanted helium.

3. Results

243
244 ^{3}He diffusion coefficients for natural monazite and the synthetic REE phosphates are
245 presented in **Tables 2 and 3** and plotted in **Figures 1 and 2**. From a least-squares fit to the data
246 for the North Carolina monazite, over the temperature range 317-600°C, we obtain an activation
247 energy of 150 ± 8 kJ/mol and pre-exponential factor (D_o) of 1.60×10^{-7} m^2/sec (log D_o = -6.797 ±
248 0.603) for diffusion normal to (100). Diffusion normal to (001) appears similar, suggesting little
249 anisotropy for He diffusion in monazite. Diffusion in the Brazil monazite, normal to (100) and
250 (010), does not differ significantly from diffusivities measured for the North Carolina monazite,
251 which suggests that differences in trace and minor element compositions of these natural
252 monazites have little effect on He diffusion. These data also reinforce the observations made for
253 the North Carolina monazite of a lack of significant anisotropy for He diffusion.
254 The time series (F**igure 3**) for the North Carolina monazite shows similar diffusivities for
255 experiments at 450ºC for durations differing by about an order of magnitude, suggesting that the
256 dominant process being measured is volume diffusion rather than transient effects that might
257 lead to time-dependence of measured diffusivities, and that diffusion behavior is consistent with
258 the assumptions made in the diffusion model. Uncertainties (2σ values shown) are comparatively
259 large for the shortest anneals because of the relatively small amounts of broadening and He loss
260 for the implanted profile for small values of Dt.
261 Fits to the data for the synthetic REE phosphates (for diffusion normal to (100)), over the
262 temperature range 300-550°C (**Figure 2**) yield activation energies of 155 ± 12, 128 ± 19, 132 ±
263 17, and 120 ± 12 kJ/mol, and pre-exponential factors of 8.77×10^{-6} (log D_o = -5.057 ± 0.946),
264 3.52×10^{-8} (log D_o = -7.454 ± 1.533), 2.25×10^{-8} (log D_o = -7.647 ± 1.336), 2.89×10^{-9} m^2/sec (log
265 D_o = -8.540 ± 0.920) for La, Nd, Sm, and Eu phosphates, respectively. He diffusivities are

somewhat faster for the lighter REE phosphates, and decrease for the heavier REE phosphates, although activation energies are higher for He diffusion in the lighter REE phosphates.

Helium diffusion also appears faster in the synthetic materials than in the natural monazite. While the results for these synthetic REE phosphates are unquestionably of interest in evaluating He transport in monazite-structure materials from a crystal-chemical perspective, it should be emphasized that, given the similarities in He diffusivities for natural monazites containing varying mixtures of rare-earth elements, as well as differences in other minor elements, the Arrhenius relation determined for natural monazite is most relevant for describing He diffusion in monazite in nature.

4. Discussion

4.1 Comparison with other He diffusion data

Previous studies have measured He diffusion in both natural monazites and synthetic monazite-structure REE phosphates. These data are summarized in **Figure 4**. Boyce et al. (2005) measured ^{4}He diffusion in the standard material Monazite 554, from the Santa Catalina Mountains of Arizona, by stepped heating of selected monazite grains. Some variability among the grains was observed, with diffusion parameters reported for the three monazite grains as follows: $E_a = 248 \pm 11$ kJ/mol, $D_o = 3.89 \times 10^{3}$ m^2/sec ($\ln(D_o/a^2) = 27.4$ sec^{-1}) for grain 3, $E_a = 179.6 \pm 1.2$ kJ/mol, $D_o = 1.29 \times 10^{-5}$ m^2/sec ($\ln(D_o/a^2) = 7.66$ sec^{-1}) for grain 4, $E_a = 216.5 \pm 4.9$ kJ/mol, and $D_o = 5.86 \times 10^{-4}$ m^2/sec ($\ln(D_o/a^2) = 11.32$ sec^{-1}) for grain 5; D_o values were calculated using grain sizes reported in Boyce et al. (2005), assuming that effective diffusion radii (a) are equivalent to grain radii. These data indicate that He diffusivities in grains 3 and 5 differ by more than 4 orders of magnitude, which the authors attribute to compositional variations (possibly substitutions of Y and/or Th for Ce) among monazite grains, and the

possible effects on He release patterns of internal zoning of U and Th. These trends roughly bracket the Arrhenius relations we have determined for natural monazites and monazite-structure synthetic rare-earth phosphates. In contrast to the findings of Boyce et al. (2005), Farley and Stockli (2002) analyzed multiple aliquots of the 554 monazite and found little intergrain variability in He diffusivities, obtaining consistent activation energies of ~200 kJ/mol and pre-exponential factors of 5.5×10^{-3} m^2/sec. Since our data suggest little dependence on He diffusion on natural monazite composition, it seems more likely that the variations in He diffusivities observed by Boyce et al. (2005) may be a consequence of nonuniform distributions of He due to internal zoning of U and Th, or possibly due to the presence of subgrain boundaries or other shortcut diffusion paths that could affect He release patterns in the bulk-release experiments of both Boyce et al. (2005) and Farley and Stockli (2002).

Farley (2007) measured He diffusion in a series of synthetic REE and Y orthophosphates (grown via a flux method using a Pb pyrophosphate flux) to explore the dependence of He diffusivity on REE phosphate composition. ^{3}He was introduced into the samples through spallogenic reactions induced by irradiation with energetic protons. ^{3}He released during stepped heating was measured to determine He diffusivities. For orthophosphates having the monazite structure, Farley (2007) observed systematic increases in activation energy for He diffusion from $LaPO_4$ - $NdPO_4$, with a slight drop in values of activation energy for $SmPO_4$ and $GdPO_4$. The activation energies and pre-exponential factors obtained for each REE phosphate were as follows: La - 183 ± 7 kJ/mol, 1.82×10^{-3} m^2/sec; Ce - 196 ± 7 kJ/mol, 2.00×10^{-2} m^2/sec; Pr - 206 ± 7 kJ/mol, 7.35×10^{-2} m^2/sec; Nd - 224 ± 8 kJ/mol, 8.96×10^{-1} m^2/sec; Sm - 215 ± 8 kJ/mol, 1.22×10^{-3} m^2/sec; Gd - 198 ± 7 kJ/mol, 3.33×10^{-5} m^2/sec. There are sharp differences among He diffusivities in the monazite-structure REE phosphates, with diffusion in $GdPO_4$ and $SmPO_4$

much slower than diffusion in $NdPO_4$, $PrPO_4$, $CePO_4$ and $LaPO_4$. Among the latter group, He diffusivities are faster for the lighter REE phosphates (with larger REE ionic radii and a more open crystal structure). Although we observe broadly similar trends of faster diffusivities for the lighter REE phosphates, and the Arrhenius trends of Farley (2007) bracket our data, the differences in He diffusivities we have measured among the monazite-structure REE orthophosphates are less pronounced than those observed by Farley (2007). In addition, we find smaller activation energies (120-155 kJ/mol) than measured in Farley's (2007) study (183-224 kJ/mol). However, if we plot all of the diffusion data from Farley's (2007) investigation, we observe that values for diffusivities determined in his study for both La and Nd phosphates are generally consistent with those measured in the present work. Farley's (2007) data for He diffusion in Gd and Sm phosphates approach our Arrhenius trends for Eu and Sm phosphates at high temperatures (~600°C).

The reasons for the quantitative differences among the He diffusivities in synthetic REE phosphates measured in our work and that of Farley (2007) are unclear. As noted in the discussion in section 4.3, there may be some anisotropy of diffusion in the end-member synthetic REE phosphates. Since the data from bulk-release experiments reflect contributions of He from the entire mineral grain, He release patterns will incorporate the effects of anisotropy (e.g., Cherniak and Watson, 2011), in contrast to data from the present study, which profiles He diffusion in a single crystallographic direction. In addition, the synthetic REE phosphates used in the two studies were grown with different fluxes. The REE phosphates used by Farley (2007) were grown with a Pb pyrophosphate flux, while those used in this work were grown with a Na_2CO_3-MoO_3 flux. Monazite growth in Pb pyrophosphate fluxes may permit heterogenous incorporation of Pb into the crystal lattice (e.g., Donovan et al., 2003) or produce Pb-rich flux

inclusions and crystals with evidence of thermomechanical stress (e.g., Boatner, 2002), which could affect diffusivities.

4.2. Potential effects of radiation damage on He diffusion

Helium diffusion may be influenced by radiation damage produced through the decay of U, Th and their daughter products. Since monazite incorporates these elements, and often in high concentrations (up to ~30 wt% ThO_2 , e.g., Overstreet 1967; Boatner and Sales 1988) it may experience changes in diffusion behavior as a consequence of this damage. Several studies indicate that monazite appears relatively resistant to radiation damage effects (e.g., Meldrum et al., 1996; Ewing and Wang, 2002); for example, monazite cannot be amorphized by bombardment with even very high does of heavy (800 keV Kr^{+}) ions at 175°C (Meldrum et al., 1998). Damage from heavy-ion bombardment at lower temperatures is annealed readily during heating for brief times (20 hours) at relatively modest temperatures (300°C) (Meldrum et al., 1996). This suggests that significant accumulation of radiation damage in monazite may not occur under many geological conditions due to self-annealing of radiation-induced defects, as also evidenced by the rarity of observations of metamict monazite in nature (e.g, Ewing et al, 1995, Ewing and Wang, 2002; Boatner and Sales, 1988; Seydoux-Guillaume et al., 2004) . Monazite-structure LREE phosphates bombarded with high dose heavy-ion irradiation are also shown to recover rapidly and achieve complete recrystallization under modest doses of electron irradiation (Meldrum et al., 1997a), indicating a strong thermodynamic driving force for recrystallization. Activation energies for recrystallization under irradiation for REE orthophosphates of monazite structure are also significantly lower than those for ABO_4 type silicates (Meldrum et al., 2000). However, although monazite may self-anneal under many conditions in nature, there is some evidence that it does not always achieve complete

363 recrystallization and repair of damage under low-temperature conditions. For example, studies of
364 monazite fission tracks (e.g., Fayon et al., 2011; Gleadow et al. 2002) indicate that tracks may
365 not fully anneal at surface temperatures over geologic timescales. In addition, Peterman et al.
366 (2012) found different dissolution rates for thermally annealed vs. untreated monazite samples,
367 suggesting the presence of radiation damage which is repaired on thermal annealing (e.g.,
368 Seydoux-Guillaume et al., 2002) .

369 In any discussion of radiation damage, it is important to distinguish between various
370 types of radiation damage, both natural and induced (for example, radiation in nature from alpha
371 recoils, fission fragments, and alpha particles, and damage induced through light or heavy ion
372 implantation or neutron irradiation), which may have significantly different effects on materials.
373 In the present study, in which we have implanted light ions at relatively low energies, radiation
374 damage from the ^{3}He implants is largely restricted to ionization (over 95% of the energy of the
375 implanted ions is dissipated in ionization effects) rather than significant displacement of lattice
376 atoms, as would occur with implantation of heavy ions, so radiation damage effects that might
377 influence diffusion should be minimal (e.g., Tesmer and Nastasi, 1995; Ziegler and Biersack,
378 2006). In addition, as has been noted by Ewing and Wang (2002), the ionization by which alpha
379 particles dissipate most of their energy causes enhanced annealing of alpha recoil damage; this
380 process can be a dominant means of recrystallization recovery, as has been demonstrated for
381 apatite (e.g., Chaumont et al., 2002), and may be the case for monazite as well.

382 Radiation damage (both natural and induced) has been proposed to slow diffusion rates in
383 apatite (Shuster et al., 2006; Shuster and Farley, 2009; Flowers et al, 2009). Shuster et al. (2006)
384 suggest that this is the result of trapping of He in defects, and possibly aggregations of He atoms
385 trapped in the manner of gas bubble inclusions. Models have been developed to attempt to

386 quantify and better understand this behavior (Shuster et al., 2006; Flowers et al., 2009),
387 incorporating the effects of accumulation and annealing of radiation damage. Although these
388 models appear to provide an explanation of apatite (U-Th)/He thermochronometric
389 measurements from a range of samples, several outstanding questions remain. While point- or
390 other localized defects may provide traps for atoms that could limit diffusion rates, extended
391 defects typically created through radiation damage (predominantly alpha recoil, which can cause
392 significant displacement of lattice atoms) would seem more likely to enhance, rather than inhibit,
393 diffusion by providing additional pathways for transport. Displacements of lattice atoms due to
394 alpha recoil effects could alter the distribution of interstitial sites by which He migrates, but it
395 seems there would be little barrier to movement of He out of extended defects if there were
396 available interstitial sites around damaged regions for He exchange and transport. It also is likely
397 in the case of apatite, for which these models have been developed and applied, that significant
398 annealing of defects may occur at modest temperatures, including conditions produced through
399 neutron irradiation used to artificially induce damage (e.g., Shuster and Farley, 2009), which
400 would add complexity to interpretations of He release patterns and estimates of diffusivities. In
401 addition, various observations, including the significantly lower helium diffusivities measured by
402 Shuster and Farley (2009) in synthetic apatite (with no radiation damage) compared with those
403 measured for Durango and other natural fluorapatites that may have sustained natural radiation
404 damage, seem difficult to reconcile with a simple conclusion that radiation damage generally
405 tends to decrease diffusivities. It is important as well to emphasize that, along with the differing
406 effects of different types of radiation, there may be differing effects on different materials
407 depending on the types of bonding in a particular mineral structure and other material

characteristics. Models developed, for example, to describe radiation damage effects in apatite, such as those outlined above, may not be directly applicable to other mineral phases.

The good agreement between the He diffusion results for the natural monazites in the present work argues against significant effects of radiation damage on diffusion in monazite, since these natural monazites differ widely in Th content, and thus in their likely degree of radiation damage. A possible explanation for the differences between He diffusivities for natural monazites and the synthetic REE phosphates may be compositional differences and their effects on directional porosity, as discussed in the next section.

4.3 Causes of variations of He diffusion among REE phosphates, natural monazites, and other mineral phases: crystals as directional molecular sieves

In previous work (Cherniak and Watson, 2011), we presented the concept of directional permeability to develop insight into why helium diffusivity should vary with lattice direction in some crystals but not in others, and to understand differences in He diffusion rates among different minerals. In the present paper, we extend this concept to evaluate REE phosphates of the monazite structure. These materials differ slightly in their lattice parameters due to differences in ionic radii of the REE, permitting exploration of the effects these differences may have on He diffusivities, with the potential as well to shed light on why diffusivities differ between the end-member synthetic REE phosphates and natural monazite which contain a mixture of REEs along with altervalent elements substituting for the rare earth elements and phosphorus.

Cherniak and Watson (2011) noted that all of the minerals that had been studied in their work on He diffusion (zircon, apatite, rutile and titanite) are highly anisotropic in their atomic structure and symmetry, but only zircon and rutile evidence appreciable diffusive anisotropy for

helium. They posited that since He — a small, unpolarized noble-gas atom — interacts minimally with the atoms in a crystal, some insight might be obtained simply by considering the size of a He atom relative to the apertures among lattice ions through which diffusive jumps might occur. This builds upon the concept of ionic porosity previously used to rationalize diffusion of noble gases in minerals (e.g., Dahl, 1996; Farley, 2007), but with the idea that ionic porosity can be a function of lattice orientation in some crystals. The specific criterion proposed by Cherniak and Watson (2011) was that He diffusivity in a given crystallographic direction depends upon the minimum (interstitial) aperture in the most densely packed planar section perpendicular to that direction, as well as the number density (i.e., the number per unit area) of those apertures in that plane. In this respect, the relevant concept might be best described as a sort of directional permeability.

Using a similar approach to Cherniak and Watson (2011), we entered ion coordinates for the minerals of interest (acquired from CrystalMaker® software, using the parameters of Ni et al. (1995) for La, Nd, Sm and Eu phosphates) into a computer program written for the purpose of creating sections through the structure at specified coordinates of one crystallographic axis. The program was used to slice through the structures of the REE phosphates in step-wise fashion, creating 2-D images of the inter-ionic space at each step. The slices were then evaluated visually to identify the most restrictive plane in the structure for each unique lattice orientation, and aperture sizes determined. These can then be compared with the commonly accepted size of the He atom (~1Å radius; e.g., Zhang and Xu, 1995; Zhang et al. 2008). Several salient observations can be made from the results for REE phosphate structures.

For monazite-structure REE phosphates, aperture sizes are largest in the $\perp c$ plane, followed by planes $\perp a$, with those $\perp b$ the smallest. There is a systematic variation in aperture size across

456 the series of REE phosphates, with apertures largest in the La phosphate, and smallest in the Sm
457 and Eu phosphates, with the Nd phosphate having intermediate values. This is generally
458 consistent with our He diffusion data for these REE phosphates, where $D_{LaPO4} > D_{NdPO4} > D_{SmPO4}$
459 $\approx D_{EuPO4}$. In addition, the aperture sizes in different planes differ less in the La phosphate than in
460 the other REE phosphates, with a difference of ~0.11 Å between aperture sizes in the $\perp c$ plane
461 and the $\perp b$ plane, compared with ~0.35-0.37 Å for the other REE phosphates. The variations in
462 aperture size suggest the possibility of anisotropy of diffusion, and potentially variations in
463 degrees of anisotropy among the REE phosphates. Unfortunately, we were unable to evaluate
464 anisotropy of diffusion for the synthetic REE phosphates because limitations in crystal
465 dimensions precluded obtaining sections in other orientations of sufficient size for analysis.
466 However, it should be noted, as pointed out in Cherniak and Watson (2011), that both the size
467 and density of the apertures may have effects on diffusivities, so that in some cases, as in titanite,
468 there may be a compensating effect between the number and size of apertures that results in little
469 or no difference in He diffusion along different directions.

470 Diffusivities of He in the synthetic REE are faster than in natural monazite, which may be a
471 consequence of the presence of several different REE with slightly differing ionic radii in the
472 natural materials, as well as substituent atoms such as Th, which may be coupled with other
473 elements to attain charge balance (e.g., Ca on the REE site or Si on the P site). These
474 substitutions of both a range of rare earth elements and other species into the mineral lattice
475 would result in greater variation in the size of apertures in the crystallographic planes, potentially
476 slowing diffusivities and decreasing the likelihood of anisotropy of diffusion when compared
477 with synthetic REE phosphates containing a single REE and no other substituent atoms.

Diffusivities of He in the synthetic REE phosphates are roughly bracketed by He diffusivities in titanite and zircon normal to c, with diffusion in $LaPO_4$ closer to He diffusion in titanite, and diffusion in $EuPO_4$ closer to that in zircon. Interestingly, the aperture sizes determined for titanite in the $\perp c$ plane (0.89 Å; Cherniak and Watson, 2011) is similar to that for the $\perp a$ plane in $LaPO_4$ (0.90 Å). For $EuPO_4$, the aperture size in this plane is somewhat larger (0.76Å) than that for the $\perp a$ plane in zircon (0.67 Å), so the findings for He diffusion in the REE phosphates appear consistent with the concept of directional permeability influencing He diffusivities.

5. Geological implications

5.1 He closure temperatures

From our diffusion data, we can calculate mean closure temperatures using the formalism of Dodson (1973; 1986). In **Figure 5a** we plot mean closure temperatures for monazite and the synthetic REE phosphate as a function of effective diffusion radius for a cooling rate of 10°C/Myr. Since there is little evidence for anisotropy of diffusion in monazite, we plot curves using spherical geometry and Arrhenius parameters for diffusion normal to (100). For comparison with our findings for natural monazite, we plot closure temperature curves using the Arrhenius relations from Boyce et al. (2005), and Farley and Stockli (2002). Because of the higher activation energy for diffusion measured in these studies – which would lead to comparatively slower diffusivities than those derived from the present work if extrapolated to lower temperatures – closure temperatures calculated with our diffusion parameters will be ~20-30°C lower than those determined from the data of Farley and Stockli (2002), and 5 to 90°C lower than those determined from the data of Boyce et al. (2005) for typical grain sizes for monazites. The closure temperatures are also within a few degrees to ~25°C of values recently

reported by Peterman et al. (2011). In **Figure 5b**, we plot closure temperature isotherms, calculated with our diffusion parameters for natural monazite, as a function of cooling rate and grain radii. For typical grain sizes and cooling rates, closure temperatures will range from ~170-210°C.

5.2. "Opening" temperatures and diffusive responses of He in monazite to heating events

While Dodson's closure temperature concept has long been used to assess the retentivity of diffusing species in minerals, its most significant limitation is that it strictly applies to cooling regimes, and was derived specifically with time-temperature paths where $T \propto 1/t$. However, many geological processes involve heating of mineral grains that are diffusively closed at the onset of heating. This is likely to be the case for He diffusion in accessory minerals, as has been noted by Reiners et al. (2005), who point out that Dodson closure temperatures can serve as "useful shorthand" for representing diffusive retentivity but have "little to no significance" for (re)heating events. Thus, in a prograde thermal regime or over a cycle of heating and cooling, it is necessary instead to consider the question of when and to what extent a mineral grain "opens up" diffusively for the diffusant of interest, rather than when closure "sets in."

Retentivity of diffusing species on heating has been considered by Cherniak and Watson (2007), who used both mathematical solutions and numerical simulations to evaluate losses of diffusant on heating from ambient conditions to nominal mean closure temperatures along a linear T-t path. Gardes and Montel (2009) derived equations for diffusive opening and for resetting of geochronological systems, but using a time-temperature path with inverse dependence of time on temperature; this is complementary to the path chosen in Dodson's (1973) derivation but may not be realistic for many geological heating scenarios.

More recently, Watson and Cherniak have extended their previous work on prograde diffusion paths to consider both linear and parabolic thermal pulses involving a full heating-cooling cycle (Watson and Cherniak, 2013; Cherniak and Watson, 2012b). Through finite-difference modeling of diffusive exchange, complemented by analytical solutions, they obtained simple expressions that relate the fraction of a diffusing species lost during a thermal event to the duration and peak temperatures of the thermal event, grain radii (a), and diffusion parameters (activation energy and pre-exponential factor) for the species of interest. In all of the examples presented below, spherical geometry of grains is considered (a reasonable assumption given typical dimensions of monazite grains, and the lack of significant anisotropy for He diffusion in natural monazite observed in this work), and samples are assumed to have a uniform initial distribution of diffusant, with no in-growth during the thermal events (which is reasonable given the duration of the heating events considered relative to ^{4}He production).

For a simple case of heating at a constant rate ($T \propto t$) Cherniak and Watson (2012b) and Watson and Cherniak (2013) showed that retention of a diffusing species is accurately described by:

$$\log \zeta = -0.457\left[\frac{E_a}{RT}\right] + \log\left[\frac{E_a D_o}{Ra^2 dT/dt}\right] - 2.3 \qquad (3)$$

with pre-exponential factor D_o in m^2/sec; activation energy Ea in J/mol; dT/dt, the heating rate, in deg/sec; a in meters; R in $J \cdot deg^{-1} mol^{-1}$; and T in Kelvin. ζ, equal to the dimensionless parameter Dt/a^2, can be directly related to the fraction of diffusant lost (F) from a sphere (Crank, 1975):

$$F = 1 - \frac{6}{\pi^2}\sum_{n=1}^{\infty}\frac{1}{n^2}\exp\left(-Dn^2\pi^2 t/a^2\right) \qquad (4)$$

In the case of non-isothermal heating, where diffusivities vary with temperature (and thus time), *Dt* will represent an integral of the diffusivity over the time of the thermal event, i.e.,:

$$\zeta = \frac{1}{a^2}\int_{t=o}^{\tau} D(t)dt \qquad (5)$$

Nonetheless, a specific value of ζ will uniquely determine F.

We can use eq. 3 above to evaluate conditions under which several (somewhat arbitrary) criteria are met: "opening", constituting 1% loss of diffusant; the "center retention" criterion, where the center of the mineral grain still retains its initial composition of diffusant (which also corresponds to ~50% loss of diffusant from the entire grain); and "resetting", which constitutes 90% loss of diffusant. Values of log ζ for these conditions are -5.056, -1.515, and -0.738, respectively. In **Figure 6**, we plot temperature conditions as a function of grain radius for each of these criteria, using a heating rate of 10°C/Myr and the diffusion parameters we have obtained for natural monazite. In the case of 50μm radius grains, diffusive opening (1% loss) will occur at 114°C, grains will still retain initial He in their centers at temperatures up to 190°C, and 90% loss will be experienced on heating to 212°C. Interestingly, the Dodson closure temperature calculated for He in 50μm radius monazite for a cooling rate of 10°C/Myr, is 187°C, very close to the maximum temperature for center retention in the monazite grain. The similarity of these values points out that in prograde thermal regimes, significant losses of diffusant can occur at temperatures well below mean closure temperatures calculated with Dodson's (1973) expression.

He retentivity for the case of paths involving both heating and cooling (starting at a low initial temperature, heating to peak temperature, and cooling back to the initial temperature) can also be evaluated (Watson and Cherniak, 2013; Cherniak and Watson, 2012b). An extension of the above linear path including both heating and cooling legs can easily be modeled, but a T-t path following a parabolic trajectory may be a more geologically realistic approximation to

thermal histories. Taking a finite-difference modeling approach similar to the above case, but with a parabolic time-temperature path, an expression can be derived relating the dimensionless parameter ζ (and therefore fractional loss of diffusant) to the diffusion parameters for the species of interest, the peak temperature (T_{pk}, in degrees K) and duration (τ, in sec) of the thermal event (time from the start of heating from initial temperature to the return to this temperature), and grain radius (a, in m):

$$\log \zeta = \log\left[\frac{D_o \tau}{a^2}\right] + \frac{140}{T_{pk}} - \frac{0.437 E_a}{R T_{pk}} - 0.8 \qquad (6)$$

In Figures 7 and 8, we present a few example calculations using eq. 6 and the He diffusion data for monazite measured in this work. In Figure 7, we plot fractional loss of He as a function of peak temperature for 80 μm monazite grains for a thermal event of 20 Myr duration. Monazite grains experiencing a peak temperature of 193°C will lose about 50% of their original He, with 5% and 90% losses for peak temperatures of 140 and 216°C, respectively. Also plotted for comparison is a curve for isothermal heating for the same duration (20 Myr) with T constant at T_{pk} rather than T a parabolic trajectory with time; the fractional losses for this case are calculated with the expression

$$\zeta = \left[\frac{D_o \tau}{a^2}\right] \exp\left(\frac{-E_a}{R T_{pk}}\right) \qquad (7)$$

For the isothermal T-t history, helium losses will be greater than for the parabolic path with equivalent peak temperature and duration, because the isothermal case will experience greater time at the highest temperature where diffusional losses are greatest.

As an example to illustrate the retentivity of He in monazite grains of various sizes experiencing a thermal history with a parabolic trajectory of heating and cooling, we plot

fractional loss of He as a function of grain radii for heating events of 2 Myr and two different peak temperatures: 170°C and 200°C (Figure 8). For a peak temperature of 170°C, 30μm diameter grains would preserve more than 50% of their initial He (and retain initial He concentrations in grain centers). If the peak temperature were 200°C, grains would have to be 100μm in diameter to retain this information. Also plotted for comparison are calculations for He loss for isothermal heating events of 2 Myr duration at temperatures of 170°C and 200°C. As noted above, the longer times at elevated temperature in the case of isothermal heating will result in greater He losses. Equivalent He losses to that for the 2 Myr parabolic path with 170°C peak temperature would be obtained for isothermal heating at 155°C, and isothermal heating at ~183°C for equivalence with the parabolic path with 200°C peak temperature.

In the above examples, we do not treat cases in which diffusant is produced over time by radioactive decay, or for mineral grains in which initial distributions of diffusing He are non-uniform due to alpha ejection. These cases can be readily addressed with numerical simulations, taking into consideration specific details suitable for modeling of a particular sample and its history, but development of generalized relationships is beyond the scope of the present paper. Nonetheless, as an illustration, we offer an example of the effects of alpha ejection profiles on fractional release of helium from monazite grains of different sizes experiencing thermal histories with different peak temperatures. The model considers a parabolic time-temperature path, with duration τ of 20 Myr. Model calculations are done with two monazite grain radii (40 and 80μm, assuming spherical grains) and peak temperatures from 125 to 225°C. The alpha ejection zone is modeled as a rim on the grain of 19μm thickness, with an initial linear gradient of He in this rim, with concentrations ranging from a value of C_o at a depth of 19μm into the grain to a value of $0.45C_o$ at the grain surface. Depths in the grain greater than 19μm will also

621 have an initial concentration of C_o. The simulations with no alpha ejection have uniform initial
622 concentrations C_o of He throughout the grain. In **Figure 9**, fractional losses (F) of He are plotted
623 as a function of time elapsed during the heating event, with simulations incorporating alpha
624 ejection compared with those for grains without ejection profiles for peak temperatures of 150°C
625 (Figure 9a,c) and 200°C (Figure 9b,d). It is evident that the effects of alpha ejection are most
626 significant for cases of small fractional losses across the T-t path; for example, in the case of
627 80μm radius grains, the absolute differences in F at the end of the parabolic path between the
628 simulations with and without alpha ejection are similar for the two peak temperatures, but the
629 relative differences in F are much larger for the simulation with T_{pk} = 150°C, where F is
630 comparatively small. This is further illustrated in Figure 10, where ΔF (the difference between
631 fractional loss with ejection, and without ejection) is plotted as a function of F (without ejection)
632 (Figure 10a) and peak temperature T_{pk} (Figure 10b). While the values for ΔF do not vary greatly
633 across the range of values of F and T_{pk} (ranging from 0 to -0.08), the relative differences will
634 only be large for smaller values of F. Hence, the effects of alpha ejection on He fractional
635 losses will be small for all but the lowest-temperature thermal events in nature, and effects on
636 laboratory-measured He release patterns would be most pronounced for low-temperature heating
637 steps.

638
639 **5.3 He diffusion in accessory minerals**
640
641 **Figure 11** shows a plot of He diffusion data for natural monazite, obtained in the present
642 study, along with titanite and rutile (Cherniak and Watson, 2011) and apatite and zircon
643 (Cherniak et al., 2009). He diffusion in monazite is slightly slower than He diffusion in zircon
644 normal to c, and falls between diffusion along the [100] and [001] directions in rutile. It is
645 considerably slower than diffusion in titanite and zircon parallel to c. He diffusion in apatite is

about five orders of magnitude faster than in monazite. Among this group of accessory minerals, activation energies for He diffusion in monazite, titanite and zircon are similar (~150 kJ/mol) while those for apatite and rutile are somewhat lower (~120 kJ/mol).

5.4 Relative retentivity of He among accessory minerals

Since we have diffusion data from a range of accessory mineral phases, we can assess the relative retentivity of He in rutile, zircon, titanite apatite and monazite. For these calculations, we use diffusion parameters for natural monazite from the present study, values for He diffusion in zircon and apatite from Cherniak et al. (2009) and Arrhenius parameters for titanite and rutile from Cherniak and Watson (2011). In **Figure 12,** we plot the fraction of He retained by each mineral as a function of time for isothermal heating at 250°C. Spherical geometry (with grain radii of 50 μm for monazite and titanite, 200 μm for apatite [because of the comparatively fast diffusion of He in apatite, a larger grain size is used so that timescales for He loss are closer to those for the other minerals]) and the analytical expression for fraction of diffusant lost from a sphere (Crank, 1975) are used for apatite, monazite and titanite since no anisotropy is observed. For rutile and zircon, cylindrical geometry (with grain radii of 50 μm and lengths of 100 μm) and the CYLMOD code for anisotropic diffusion in a cylinder (Watson et al., 2010) are used to calculate fractional He loss given the anisotropy of diffusion in these minerals (two orders of magnitude difference in D for diffusion parallel and normal to c for both zircon and rutile; Cherniak et al., 2009; Cherniak and Watson, 2011). For grains of roughly equivalent size, monazite would be most retentive of He, followed by rutile, zircon and titanite. Apatite is much less retentive of He (e.g., Cherniak et al., 2009; Farley, 2000) than the other accessory mineral phases.

Conclusion

He diffusion has been measured in natural monazite and synthetic monazite-structure REE phosphates using ion implantation to introduce ^{3}He and nuclear reaction analysis to measure ^{3}He in samples following diffusion anneals. For diffusion in natural monazite we obtain the following Arrhenius relation for diffusion normal to (100):

$D = 1.60 \times 10^{-7} \exp(-150 \pm 8 \text{ kJ mol-1}/RT)\ m^2 sec^{-1}$.

Diffusion in natural monazite exhibits little diffusional anisotropy, and diffusivities of He in natural monazites from two different localities are similar. The similarities in He diffusivities for these natural monazites containing different proportions of rare-earth elements, as well as differing Th contents, indicate that this Arrhenius relation is most relevant for describing He diffusion in monazite in nature. Over the investigated temperature range, these diffusivities are similar to those of Farley and Stockli (2002), and values obtained for some measurements of natural monazite crystals by Boyce et al. (2005), and are bracketed by diffusivities obtained by Farley (2007) for monazite-structure synthetic REE phosphates.

He diffusion in synthetic REE phosphates ($LaPO_4$, $NdPO_4$, $SmPO_4$ and $EuPO_4$) with the monazite structure appears to behave systematically, with diffusion in the lighter REE phosphates slightly faster than in the heavier REE phosphates. This trend is in broad agreement with the findings of Farley (2007), but the difference in diffusivities among the REE phosphates is smaller than that reported in Farley's (2007) work. Activation energies for He diffusion in the synthetic LREE phosphates are similar to that for natural monazite measured in this study, but He diffusivities in synthetic $LaPO_4$ are about an order of magnitude faster than in the natural monazites. The differences in He diffusivities among the natural monazites and synthetic REE phosphates may be a consequence of "directional porosity" -- the density and distribution of

interstitial apertures in the crystal structure, which may result in differences in He migration rates.

The Arrhenius relation determined in this work is used to evaluate He retentivity in monazite experiencing thermal events, using both Dodson's (1973) closure temperature formulation and recently developed expressions (Watson and Cherniak, 2013) for prograde thermal events and heating and cooling trajectories, derived from finite difference modeling and mathematical treatments. The finite difference models developed by Watson and Cherniak (2013) can also be modified to incorporate the effects of alpha ejection; these effects are minor for all cases except in instances of very low-temperature heating and concomitant small He losses. These examples, along with calculations using diffusion parameters determined for He diffusion in other accessory minerals, indicate that monazite is comparatively retentive of He.

Acknowledgements – Thanks to Richard Ketchum and an anonymous reviewer for their review comments, which aided significantly in improving the final version of the paper, and to Gregory Dumond for editorial handling. We also thank Greg Dumond and Callum Hetherington for their efforts in organizing the GSA special session on monazite and its companion virtual special issue in American Mineralogist. We thank Michihiko Nakamura, Joe Pyle, and Dan Ruscitto for monazite samples and analyses, and Wayne Skala for assistance with ion implantation. This work was supported by grant EAR-0948204 from the National Science Foundation (to E.B.Watson).

720 **References**
721
722 Boatner, L.A. and Sales, B.C. (1988) Monazite. In W. Lutze and R.C. Ewing, Eds., Radioactive
723 Waste Forms for the Future, p. 495–564. North Holland, Amsterdam.
724
725 Boyce, J. W., Hodges, K.V., Olszewski, W. J., and Jercinovic, M.J. (2005) He diffusion in
726 monazite; implications for (U-Th)/He thermochronometry. Geochemistry, Geophysics,
727 Geosystems, 6.
728
729 Chaumont, J., Soulet, S., Krupa, J.C., and Carpena, J. (2002) Competition between disorder
730 creation and annealing in fluorapatite nuclear waste forms. Journal of Nuclear Materials, 301,
731 122-128.
732
733 Cherniak, D.J. and Watson, E.B. (2007) Ti diffusion in zircon. Chemical Geology, 242, 473-483.
734
735 Cherniak, D.J. and Watson, E.B. (2011) Helium diffusion in rutile and titanite, and consideration
736 of the origin and implications of diffusional anisotropy. Chemical Geology, 288, 149-161.
737
738 Cherniak, D.J. and Watson E.B. (2012a) Helium diffusion in olivine at 1 atm and 2.7 GPa.
739 Geochimica et Cosmochimica Acta, 84, 269–279.
740
741 Cherniak, D.J. and Watson E.B. (2012b) Diffusion in Minerals Relevant to Geochronology. 22nd
742 V.M. Goldschmidt Conference. Geochemical Society.
743
744 Cherniak, D.J., Watson, E.B., and Thomas, J.B. (2009) He diffusion in zircon and apatite.
745 Chemical Geology, 268, 155-166.
746
747 Cherniak, D.J., Watson, E.B., Grove, M., and Harrison, T.M. (2004a) Pb diffusion in monazite:
748 a combined RBS/SIMS study. Geochimica et Cosmochimica Acta, 68, 829-840.
749
750 Cherniak, D.J., Zhang, X.Y., Nakamura, M., and Watson, E.B. (2004b) Oxygen diffusion in
751 monazite. Earth and Planetary Science Letters, 226, 161-174.
752
753 Cherniak, D.J., Pyle, J., and Rakovan, J. (2004c) Synthesis of REE and Y phosphates by Pb-free
754 flux methods, with utilization as standards for electron microprobe analysis, and in design of
755 monazite chemical U-Th-Pb dating protocol. American Mineralogist, 89, 1533-1539.
756
757 Costantini, J.-M., Trocellier, P., Haussy, J., and Grob, J.-J. (2002) Nuclear reaction analysis of
758 helium diffusion in britholite Nuclear Instruments and Methods, B195, 400-407.
759
760 Costantini, J.-M., Grob, J.-J., Haussy, J., Trocellier, P., and Trouslard, P. (2003) Nuclear reaction
761 analysis of helium migration in zirconia. Journal of Nuclear Materials, 321, 281-287.
762
763 Crank, J. (1975) The Mathematics of Diffusion, 2nd edn. Oxford University Press.
764

765 Dahl, P.S. (1996) The effects of composition on retentivity of argon and oxygen in hornblende
766 and related amphiboles: a field-tested empirical model. Geochimica et Cosmochimica Acta, 60,
767 3687-3700.

768 Dieumegard, D., Dubreuil, D., and Amsel, G. (1979) Analysis and depth profiling of deuterium
769 with the D(^{3}He,p)^{4}He reaction by detecting the protons at backward angles. Nuclear Instruments
770 and Methods, 166, 431-445.
771
772 Dodson, M.H. (1973) Closure temperatures in cooling geological and petrological systems.
773 Contributions to Mineralogy and Petrology, 40, 259-274.
774
775 Dodson, M.H. (1986) Closure profiles in cooling systems. Materials Science Forum, 7, 145-154.
776
777 Donovan, J.J., Hanchar, J.M., Picolli, P.M., Schrier, M.D., Boatner, L.A. and Jarosewich, E.
778 (2003) A re-examination of the rare-earth-element orthophosphate standards in use for electron-
779 microprobe analysis. Canadian Mineralogist, 41, 221-232.
780
781 Ehlers, T. A. and Farley, K. A. (2003) Apatite (U-Th)/He thermochronometry; methods and
782 applications to problems in tectonic and surface processes. Earth and Planetary Science Letters,
783 206, 1-14.
784
785 Ewing, R. C. and Wang, L.-M. (2002) Phosphates as nuclear waste forms. In M.J. Kohn, J.
786 Rakovan, J.M. Hughes, Eds., Phosphates: geochemical, geobiological, and materials importance.
787 Reviews in Mineralogy and Geochemistry, Vol. 48, pp.673-699. Mineralogical Society of
788 America and Geochemical Society.
789
790 Ewing, R.C., Weber, W.J., and Clinard, F.W. Jr. (1995) Radiation effects in nuclear waste forms
791 for high-level radioactive waste. Progress in Nuclear Energy, 29, 63-127.
792
793 Farley, K.A. (2002) (U-Th)/He dating: Techniques, calibrations and applications. In D. Porcelli,
794 C.J. Ballentine, and R. Wieler, Eds., Noble Gases in Geochemistry and Cosmochemistry,
795 Reviews in Mineralogy and Geochemistry, Vol. 47, pp. 819-844. Mineralogical Society of
796 America and Geochemical Society.
797
798 Farley, K.A. (2000) Helium diffusion from apatite: General behavior as illustrated by Durango
799 fluorapatite. Journal of Geophysical Research, 105, 2903-2914.
800
801 Farley, K.A. (2007) He diffusion systematics in minerals: Evidence from synthetic monazite and
802 zircon structure phosphates. Geochimica et Cosmochimica Acta, 71, 4015-4024.

803 Farley, K.A. and Stockli, D.F., 2002. (U-Th)/He dating of phosphates: apatite, monazite, and
804 xenotime. In D. Porcelli, C.J. Ballentine, R. Wieler, Eds., Noble Gases in Geochemistry and
805 Cosmochemistry, Reviews in Mineralogy and Geochemistry, Vol. 47, pp. 559-577.
806 Mineralogical Society of America and Geochemical Society.
807

Fayon, A., Gombosi, D. J., and Ruscitto, D. (2011) Fission track dating of monazite; etching efficiencies as a function of U content. Abstracts with Programs - Geological Society of America Annual Meeting, 43, 331.

Flowers, R.M., Ketcham, R.A., Shuster, D.L., and Farley, K.A. (2009) Apatite (U-Th)/He thermochronometry using a radiation damage accumulation and annealing model. Geochimica et Cosmochimica Acta, 73, 2347-2365.

Gardes, E., and Montel, J.-M. (2009) Opening and resetting temperatures in heating geochronological systems. Contributions to Mineralogy and Petrology, 158, 185-195.

Gleadow, A.J.W., Belton, D.X., Kohn, B.P., and Brown, R.W. (2002) Fission track dating of phosphate minerals and the thermochronology of apatite. Reviews in Mineralogy and Geochemistry, 48: 579-630.

Gosset, D., Trocellier, P., and Serruys, Y. (2002) Determination of the helium diffusion coefficient in nuclear waste , storage ceramics by a nuclear reaction analysis method. Journal of Nuclear Materials, 303, 115-124.

Gosset, D. and Trocellier, P. (2005) Determination of the helium thermal diffusion coefficient in britholite using a NRA method: new results. Journal of Nuclear Materials, 336, 140-144.

Hodges, K., van Soest, M. C., Monteleone, B. D., and Boyce, J. W. (2009) Direct evidence for anisotropic He diffusivity in zircon provided by laser depth profiling. AGU Fall Meeting 2009, abstract #V52C-04

House, M.A., Wernicke, B.P., and Farley, K.A. (1998) Dating topography of the Sierra Nevada, California, using apatite (U-Th)/He ages. Nature, 396, 66-69.

House, M. A., Wernicke, B. P., Farley, K. A., and Dumitru, T. A. (1997) Cenozoic thermal evolution of the central Sierra Nevada, California, from (U-Th)/He thermochronometry. Earth and Planetary Science Letters, 151, 167-179.

Ketcham, R.A., Guenthner, W.R., and Reiners, P.W. (2013) Geometric analysis of radiation damage connectivity in zircon, and its implications for helium diffusion. American Mineralogist, 98, 350-360.

Kohn, M. and Malloy, M. A. (2004) Formation of monazite via prograde metamorphic reactions among common silicates; implications for age determinations. Geochimica et Cosmochimica Acta, 68, 101-113.

Mayer, M., Alimov, V.K., and Roth, J. (2005) Differential cross-section of the $D(^3He,p)^4He$ nuclear reaction and depth profiling of deuterium up to large depths. Nuclear Instruments and Methods, B234, 169-175.

Meldrum, A., Wang, L.M., and Ewing, R.C. (1996) Ion beam induced amorphization of monazite. Nuclear Instruments and Methods, B116, 220-224.

Meldrum, A., Boatner, L.A., and Ewing, R.C. (1997b) Displacive radiation effects in the monazite- and zircon-structure orthophosphates. Physical Review, B56, 13805-13814.

Meldrum, A., Boatner, L.A., and Ewing, R.C. (1997a) Electron-irradiation-induced nucleation and growth in amorphous $LaPO_4$, $ScPO_4$, and zircon. Journal of Materials Science, 12, 1816-1827.

Meldrum, A., Boatner, L.A., Weber, W.J., and Ewing, R.C. (1998) Radiation damage in zircon and monazite. Geochimica et Cosmochimica Acta, 62, 2509-2520.

Meldrum, A., Boatner, L.A., and Ewing, R.C. (2000) A comparison of radiation effects in crystalline ABO_4 -type phosphates and silicates. Mineralogical Magazine, 64, 185-194.

Miro, S., Studer, F., Costantini, J.-M., Haussy, J., Trouslard, P., and Grob, J.-J. (2006) Effect of composition on helium diffusion in fluoroapatites investigated with nuclear reaction analysis. Journal of Nuclear Materials, 355, 1-9.

Miro, S., Studer, F., Costantini, J.-M., Berger, P., Haussy, J., Trouslard, P., and Grob, J.-J. (2007) Effect of gold ion irradiation on helium migration in fluorapatites investigated with nuclear reaction analysis. Journal of Nuclear Materials, 362, 445-450.

Möller, W. and Besenbacher, F. (1980) A note on the ^{3}He+D nuclear-reaction cross section. Nuclear Instruments and Methods, 168, 111-114.

Ni, Y., Hughes, J.M., and Mariano, A.N. (1995) Crystal chemistry of the monazite and xenotime structures. American Mineralogist, 80, 21-26.

Ouchani, S., Dran, J.-C., and Chaumont, J. (1998) Exfoliation and diffusion following helium ion implantation in fluorapatite: implications for radiochronology and radioactive waste disposal. Applied Geochemistry, 13, 707-714.

Overstreet, W.C. (1967) The geologic occurrence of monazite. US Geological Survey Professional Paper, 530, 327 p.

Paszti, F. (1992) Microanalysis of He using charged particle accelerators. Nuclear Instruments and Methods, B66, 83-106.

Payne, R.S., Clough, A.S., Murphy, P., and Mills, P.J. (1989) Use of the D(^{3}He,p)^{4}He reaction to study polymer diffusion in polymer melts. Nuclear Instruments and Methods, B42, 130-134.

Peterman, E.M., Grove, M., and Hourigan, J. (2011) Development and intercalibration of monazite (U-Th)/ He thermochonology: Catnip Sill, Catalina Core Complex. Paper #130-11, 2011 GSA Annual Meeting

Peterman, E.M., Mattinson, J.M., and Hacker, B.R. (2012) Multi-step TIMS and CA-TIMS monazite U–Pb geochronology. Chemical Geology 312–313, 58–73

Pronko, P.P. and Pronko. J.G. (1974) Depth profiling of ^{3}He and ^{2}H in solids using the ^{3}He(d,p)^{4}He resonance. Physical Review, B9, 2670-2678.

Pyle, J.M., Spear, F.S., Rudnick, R.L., McDonough, W. F. (2001) Monazite-xenotime-garnet equilibrium in metapelites and a new monazite-garnet thermometer. Journal of Petrology, 42, 2083-2107.

Reiners, P.W. and Farley, K.A. (2001) Influence of crystal size on apatite (U-Th)/He thermochronology: an example from the Bighorn Mountains, Wyoming. Earth and Planetary Science Letters, 188, 413-420.

Reiners, P.W., Brady, R., Farley, K. A., Fryxell, J. E., Wernicke, B., and Lux, D. (2000) Helium and argon thermochronometry of the Gold Butte Block, South Virgin Mountains, Nevada. Earth and Planetary Science Letters, 178, 315-326.

Reiners, P.W., Farley, K. A., and Hickes, H. J. (2002) He diffusion and (U-Th)/He thermochronometry of zircon; initial results from Fish Canyon Tuff and Gold Butte. Tectonophysics, 349, 297-308.

Reiners, P.W., Spell, T. L., Nicolescu, S., and Zanetti, K. A. (2004) Zircon (U-Th)/He thermochronometry; He diffusion and comparisons with ^{40}Ar/ ^{39}Ar dating. Geochimica et Cosmochimica Acta, 68, 1857-1887.

Reiners, P.W., Ehlers, T.A., and Zeitler, P.K. (2005) Past, present, and future of thermochronology. In: P.W. Reiners, P.W. and T.A. Ehlers, Eds., Low-temperature Thermochronology: Techniques, Interpretations, and Applications. Reviews in Mineralogy and Geochemistry, Vol. 58, pp.1-18. Mineralogical Society of America and Geochemical Society, Washington, DC.

Roselieb, K., Rauch, F., Dersch, O., and Buttner, H. (2006) Diffusivity and solubility of He in garnet: An exploratory study using nuclear reaction analysis. Nuclear Instruments and Methods, B244, 412-418.

Ryssel, H. and Ruge, I. (1986) Ion Implantation. John Wiley, New York.

Seydoux-Guillaume, A.-M., Wirth, R., Deutsch, A., and Schärer, U. (2004) Microstructure of 24-1928 Ma concordant monazites; implications for geochronology and nuclear waste deposits. Geochimica et Cosmochimica Acta, 68, 2517-2527.

Seydoux-Guillaume, A.-M, Wirth, R., Nasdala, L., Gottschalk, M., Montel, J.N, and Heinrich, W. (2002) XRD, TEM and Raman study of experimental annealing of natural monazite. Physics and Chemistry of Minerals, 29, 240–253.

Shannon, R.D. (1976) Revised effective ionic radii and systematic studies of interatomic distances in halides and chalcogenides. Acta Crystallographica, A32, 751-767.

Shannon, R.D. and Prewitt, C.T. (1969) Effective ionic radii in oxides and fluorides. Acta Crystallographica, B 25, 925-946.

Shuster, D. L. and Farley, K. A. (2009) The influence of artificial radiation damage and thermal annealing on helium diffusion kinetics in apatite. Geochimica et Cosmochimica Acta, 73, 183-196.

Shuster, D. L. and Farley, K. A. (2005a) $^{4}He/^{3}He$ thermochronometry; theory, practice, and potential complications. In P.W. Reiners, T.A. Ehlers, Eds., Low-temperature Thermochronology: Techniques, Interpretations, and Applications. Reviews in Mineralogy and Geochemistry, Vol. 58, pp.181-203. Mineralogical Society of America and Geochemical Society, Washington, DC.

Shuster, D.L. and Farley, K.A. (2005b) Diffusion kinetics of proton-induced Ne-21, He-3, and He-4 in quartz. Geochimica et Cosmochimica Acta, 69, 2349-2359.

Shuster, D.L. and Farley, K.A. (2004) $^{4}He/\ ^{3}He$ thermochronometry , Earth and Planetary Science Letters, 217, 1-17.

Shuster, D.L., Farley, K.A., Sisterson, J.M., and Burnett, D.S. (2004) Quantifying the diffusion kinetics and spatial distribution of radiogenic ^{4}He in minerals containing proton-induced ^{3}He. Earth and Planetary Science Letters, 217, 19-32.

Shuster, D.L., Flowers, R.M., and Farley, K.A. (2006) The influence of natural radiation damage on helium diffusion kinetics in apatite. Earth and Planetary Science Letters, 249, 148-161.

Stockli, D.F. (2005) Application of low-temperature thermochronometry to extensional tectonic settings. In P.W. Reiners and T.A. Ehlers, Eds., Low-temperature Thermochronology: Techniques, Interpretations, and Applications. Reviews in Mineralogy and Geochemistry, Vol. 58, pp.411-448. Mineralogical Society of America and Geochemical Society, Washington, DC.

Stockli, D. F., Farley, K. A., Walker, J. D., and Blackburn, T. J. (2005) He diffusion and (U-Th)/He thermochronometry of monazite and rutile. Geochimica et Cosmochimica Acta, 69, Issue 10, Suppl. 8

Tesmer, J.R. and Nastasi, M. (1995) Handbook of Modern Ion Beam Materials Analysis. Materials Research Society, Pittsburgh, PA.

Trocellier, P., Gosset, D., Simeone, D., Costantini, J.M., Deschanels, X., Roudil, D., Serruys, Y., Grynszpan, R., Saudé, S., and Beauvy, M. (2003a) Application of nuclear reaction geometry for ^{3}He depth profiling in nuclear ceramics. Nuclear Instruments and Methods, B206, 1077-1082.

Trocellier, P., Gosset, D., Simeone, D., Costantini, J.-M., Deschanels, X., Roudil, D., Serruys, Y., Grynszpan, R., Saudé, S., and Beauvy, M. (2003b) ^{3}He thermal diffusion coefficient measurement in crystalline ceramics by μNRAdepth profiling. Nuclear Instruments and Methods, B210, 507-512.

van Soest, M., Monteleone, B.D., Hodges, K.V., and Boyce, J.W. (2011) Laser depth profiling studies of helium diffusion in Durango fluorapatite. Geochimica et Cosmochimica Acta, 75, 2409-2419.

Watson, E.B. and Cherniak D.J. (2013) Simple equations for diffusion in response to heating. Chermical Geology, 355, 93-104.

Watson, E.B., Wanser, K.H., and Farley, K.A. (2010) Anisotropic diffusion in a finite cylinder, with geochemical applications. Geochimica et Cosmochimica Acta, 74, 614-633.

Wolf, R.W., Farley, K.A., and Kass, D.M. (1998) Modeling of the temperature sensitivity of the apatite (U-Th)/He thermochronometer. Chemical Geology, 148, 105-114.

Wolf, R.W., Farley, K.A., and Silver, L.T. (1996) Assessment of (U-Th)-He thermochronometry: The low-temperature history of the San Jacinto Mountains, California. Geology, 25, 65-68.

Yang, P. and Pattison, D. (2006) Genesis of monazite and Y zoning in garnet from the Black Hills, South Dakota. Lithos, 88, 233-253.

Zhang, L., Van Orman, J.A., and Lacks, D.J. (2008) Effective radii of noble gas atoms in silicates from first-principles molecular simulation. American Mineralogist, 94, 600-608.

Zhang, Y. and Xu, Z. (1995) Atomic radii of noble gas elements in condensed phases. American Mineralogist, 80, 670-675.

Ziegler, J.F. and Biersack, J.P. (2006) The stopping and range of ions in matter. Computer code SRIM 2006, http://www.srim.org.

1024 **Table 1. Compositional analysis of natural monazites used**
1025 **in this study.**

	North Carolina monazite	Brazil monazite
P_2O_5	30.40 (0.34)	27.74 (0.21)
SiO_2	0.40 (0.17)	1.53 (0.06)
CaO	0.18 (0.17)	0.52 (0.02)
PbO	0.03 (0.02)	0.23 (0.02)
ThO_2	1.28 (1.24)	7.66 (0.41)
UO_2	0.10 (0.04)	0.29 (0.07)
Y_2O_3	0.74 (0.16)	0.45 (0.01)
La_2O_3	15.22 (0.96)	14.40 (0.17)
Ce_2O_3	31.12 (1.03)	29.26 (0.44)
Pr_2O_3	4.05 (0.99)	5.05 (0.08)
Nd_2O_3	12.33 (0.79)	10.34 (0.18)
Sm_2O_3	2.19 (0.44)	2.19 (0.05)
Gd_2O_3	1.46 (0.42)	0.89 (0.04)
Tb_2O_3	0.12 (0.04)	0.03 (0.03)
Dy_2O_3	0.36 (0.06)	0.23 (0.02)
Er_2O_3	0.03 (0.02)	0.01 (0.01)
Total	100.01	100.83

1026 Measurements are wt% oxides, by electron microprobe, with
1027 multiple (7-10) point analyses of grains. Standard deviations
1028 are in parentheses.
1029
1030
1031

1032 Table 2. ^{3}He Diffusion in Natural Monazite

	T(°C)	*time(sec)*	*D(m^2sec^{-1})*	*log D*	*+/-*
1033 *North Carolina Monazite (100):*					
He3EMZ-9	600	$1.80x10^{3}$	$1.17x10^{-17}$	-15.93	0.34
He3EMZ-3	549	$1.80x10^{3}$	$2.74x10^{-17}$	-16.56	0.36
He3EMZ-4	500	$4.20x10^{3}$	$1.69x10^{-17}$	-16.77	0.18
He3EMZ-5	452	$1.08x10^{4}$	$3.81x10^{-18}$	-17.42	0.28
He3EMZ-6	452	$4.50x10^{3}$	$4.64x10^{-18}$	-17.33	0.44
He3EMZ-8	454	$4.68x10^{4}$	$1.91x10^{-18}$	-17.72	0.12
He3EMZ-1	401	$7.56x10^{4}$	$6.22x10^{-19}$	-18.21	0.35
He3EMZ-7	354	$5.08x10^{5}$	$5.91x10^{-20}$	-19.23	0.31
He3EMZ-2	317	$3.63x10^{6}$	$6.01x10^{-21}$	-20.22	0.27
1034 *North Carolina Monazite (001):*					
He3EMZ-15	550	$1.20x10^{3}$	$6.90x10^{-17}$	-16.16	0.32
He3EMZ-11	498	$4.50x10^{3}$	$6.69x10^{-18}$	-17.17	0.44
He3EMZ-10	446	$2.52x10^{4}$	$1.98x10^{-18}$	-17.70	0.35
He3EMZ-12	402	$1.60x10^{5}$	$4.68x10^{-19}$	-18.33	0.30
He3EMZ-13	352	$1.28x10^{6}$	$5.12x10^{-20}$	-19.29	0.43
1035 *Brazil Monazite (010):*					
He3BrMz-5	550	$1.20x10^{3}$	$3.42x10^{-17}$	-16.47	0.19
He3BrMz-2	498	$4.50x10^{3}$	$1.68x10^{-17}$	-16.78	0.10
He3BrMz-1	446	$2.52x10^{4}$	$2.64x10^{-18}$	-17.58	0.15
He3BrMz-3	402	$1.60x10^{5}$	$5.37x10^{-19}$	-18.27	0.11
He3BrMz-4	352	$1.28x10^{6}$	$2.36x10^{-20}$	-19.63	0.35
1036 *Brazil Monazite (100):*					
He3BrMz-11	550	$1.20x10^{3}$	$5.95x10^{-17}$	-16.23	0.23
He3BrMz-6	501	$5.40x10^{3}$	$8.54x10^{-18}$	-17.07	0.16
He3BrMz-7	453	$2.64x10^{4}$	$1.78x10^{-18}$	-17.75	0.08
He3BrMz-10	395	$2.36x10^{5}$	$2.87x10^{-19}$	-18.54	0.22
He3BrMz-8	346	$1.29x10^{6}$	$2.82x10^{-20}$	-19.55	0.20

1037
1038

Table 3. ^{3}He Diffusion in Synthetic REE Phosphates

	T(°C)	*time(sec)*	*D(m^2sec^{-1})*	*log D*	*+/-*
$LaPO_4$:					
He3LaPO4-3	501	$9.00x10^{2}$	$3.38x10^{-16}$	-15.51	0.21
He3LaPO4-4	450	$1.50x10^{3}$	$7.98x10^{-17}$	-16.26	0.26
He3LaPO4-1	403	$1.73x10^{5}$	$5.13x10^{-18}$	-17.29	0.31
He3LaPO4-2	357	$8.64x10^{4}$	$1.48x10^{-18}$	-17.83	0.27
He3LaPO4-5	300	$6.91x10^{5}$	$5.86x10^{-20}$	-19.23	0.22
$NdPO_4$:					
He3NdPO4-3	501	$9.00x10^{2}$	$1.01x10^{-16}$	-16.00	0.41
He3NdPO4-4	450	$1.50x10^{3}$	$2.65x10^{-17}$	-16.58	0.41
He3NdPO4-1	404	$1.73x10^{5}$	$2.67x10^{-18}$	-17.57	0.25
He3NdPO4-2	350	$6.48x10^{4}$	$9.03x10^{-19}$	-18.04	0.27
He3NdPO4-5	299	$9.65x10^{5}$	$6.19x10^{-20}$	-19.21	0.34
$SmPO_4$:					
He3SmPO4-3	501	$1.20x10^{3}$	$3.16x10^{-17}$	-16.50	0.35
He3SmPO4-4	450	$5.40x10^{3}$	$8.13x10^{-18}$	-17.09	0.34
He3SmPO4-1	403	$1.73x10^{5}$	$9.46x10^{-19}$	-18.02	0.29
He3SmPO4-2	350	$3.46x10^{5}$	$2.16x10^{-19}$	-18.67	0.28
He3SmPO4-5	299	$9.65x10^{5}$	$2.14x10^{-20}$	-19.67	0.29
$EuPO_4$:					
He3EuPO4-3	501	$1.20x10^{3}$	$2.58x10^{-17}$	-16.59	0.24
He3EuPO4-4	450	$3.30x10^{3}$	$6.30x10^{-18}$	-17.20	0.22
He3EuPO4-1	403	$1.73x10^{5}$	$1.15x10^{-18}$	-17.94	0.29
He3EuPO4-2	357	$8.64x10^{4}$	$2.88x10^{-19}$	-18.54	0.36
He3EuPO4-5	300	$6.91x10^{5}$	$3.59x10^{-20}$	-19.45	0.19

Captions for Figures

Figure 1. Arrhenius plot for helium diffusion in natural monazite. From a fit to the data for diffusion for the North Carolina monazite (diffusion normal to (100)) (black circles) an activation energy of 150 ± 8 kJ/mol and pre-exponential factor (D_o) of 1.60×10^{-7} m^2/sec ($\log D_o = -6.797 \pm 0.603$) are obtained. Diffusion the North Carolina monazite normal to (001) (grey circles) appears similar, as are data for diffusion in another natural monazite for diffusion normal to (100) and (010) (white and grey squares, respectively), suggesting little dependence on crystallographic orientation for He diffusion in monazite.

Figure 2. Arrhenius plot for helium diffusion in synthetic REE phosphates. Fits to the data for the synthetic REE phosphates (for diffusion normal to (100)), over the temperature range 300-550°C yield activation energies of 155 ± 12, 128 ± 19, 132 ± 17, and 120 ± 12 kJ/mol, and pre-exponential factors of 8.77×10^{-6} ($\log D_o = -5.057 \pm 0.946$), 3.52×10^{-8} ($\log D_o = -7.454 \pm 1.533$), 2.25×10^{-8} ($\log D_o = -7.647 \pm 1.336$), 2.89×10^{-9} m^2/sec ($\log D_o = -8.540 \pm 0.920$) for La, Nd, Sm, and Eu phosphates, respectively.

Figure 3. Time series for He diffusion in natural monazite. He diffusivities are within experimental uncertainty for diffusion anneals of durations ranging over an order of magnitude at 450°C, suggesting that volume diffusion of He is the dominant process being measured. Also evident are the similarities in diffusivities for natural monazites from different localities, and for different crystallographic orientations.

Figure 4a. Summary of measurements of diffusion of He in natural monazite, comparing the findings from the present study with reported Arrhenius relations from step-heating experiments of Farley and Stockli (2002) and Boyce et al. (2005) for the 554 Monazite from the Santa Catalina Mountains of Arizona, by stepped heating of selected monazite grains. Boyce et al. (2005) observe some variability among the grains they studied (numbered #3, #4 and #5), with He diffusivities differing by more than 4 orders of magnitude; these trends roughly bracket our Arrhenius relation for natural monazites. In contrast, Farley and Stockli (2002) analyzed multiple aliquots of the 554 monazite and found little intergrain variability in He diffusivities; their diffusivities are faster than those obtained in the present study, but with a higher activation energy for diffusion.

Figure 4b. Summary of measurements for He diffusion in synthetic REE phosphates of monazite structure, comparing data from the present study with results from the stepped heating studies of Farley (2007) (lines indicated by (F) in figure). Farley (2007) finds sharp differences among He diffusivities in the monazite-structure REE phosphates, with diffusion in $GdPO_4$ and $SmPO_4$ much slower than diffusion in $NdPO_4$ and $LaPO_4$. Among the latter group, He diffusivities are faster for the lighter REE phosphates (with larger REE ionic radii and a more open crystal structure). Although we find broadly similar trends of faster diffusivities for the lighter REE phosphates, the differences are less pronounced than those observed by Farley (2007).

Figure 5. Mean closure temperatures for monazite and synthetic monazite-structure orthophosphates as a function of effective diffusion radius for a cooling rate of 10°C/Myr, using the expression of Dodson (1973). In (a), we plot curves using spherical geometry and Arrhenius parameters obtained in this study for natural monazite normal to (100). For comparison, closure temperature estimates for monazite from Boyce et al. (2005) (using their Arrhenius relations for

grains #3, #4 and #5, plotted in the previous figure) and Farley and Stockli (2002) are shown. In **(b)**, we plot closure temperature isotherms, calculated with our diffusion parameters for natural monazite, as a function of cooling rate and grain radii. For typical grain sizes and cooling rates, closure temperatures will range from ~170-210°C.

Figure 6. Diffusive "opening", "resetting" and "center retention" criteria for helium in monazite grains heated at a linear rate of 10°C/Myr, calculated using eq.3. Conditions for "opening" (1% loss of diffusant); "center retention" criterion (where the center of the mineral grain still retains its initial concentration of diffusant); and "resetting" (90% loss of diffusant) are plotted as a function of maximum heating temperature and grain radius. In the case of 50μm radius grains, diffusive opening will occur at 114°C, grains will still retain initial He in their centers at temperatures up to 190°C, and resetting will be experienced at 212°C. See text for additional discussion.

Figure 7. Plot of fractional loss of He as a function of peak temperature for 80 μm grains for a thermal event of 20 Myr duration and parabolic trajectory, calculated using eq. 6. Monazite grains experiencing a peak temperature of 193°C will lose about 50% of their original He, with 5% and 90% losses for peak temperatures of 140 and 216°C, respectively. Also plotted for comparison is a curve for isothermal heating for the same duration (20 Myr) with temperature constant at T_{pk} rather than following a parabolic trajectory with time. Helium losses will be greater for the isothermal T-t history than for the parabolic path with the same peak temperature and duration, because the isothermal example will experience a longer time at the highest temperature where diffusional losses are greatest.

Figure 8. Plot of fractional loss of He as a function of grain radii for heating events of 2 Myr and two different peak temperatures (170°C and 200°C), illustrating the retentivity of He in monazite grains of various sizes when experiencing a parabolic trajectory of heating and cooling. For a peak temperature of 170°C, 30μm diameter grains would preserve more than 50% of their initial He (and retain initial He concentrations in grain centers), while grains of 100μm diameter would experience equivalent retention for peak temperatures of 200°C. Curves are calculated using eq. 6 and diffusion parameters for He in natural monazite measured in this study. Also plotted for comparison are calculations for He loss for isothermal heating events of 2 Myr duration at temperatures of 170°C and 200°C (dashed lines). Because of the longer times at elevated temperatures for the case of isothermal heating, He losses will be greater.

Figure 9. Plots of fractional loss of He for 40um (a,b) and 80um (c,d) monazite grains, comparing He losses for grains modeled with and without the effects of alpha ejection. A parabolic T-t path of 20 Myr duration is used in the models, with peak temperatures of 150 (a,c) and 200 (b,d). The effects of alpha ejection are most pronounced for T-t paths with small fractional losses of He. See text for additional discussion.

Figure 10. Plot of ΔF (the difference between fractional loss with ejection, and without ejection) as a function of F (without ejection) (a) and peak temperature T_{pk} (b). While the values for ΔF do not vary greatly across the range of values of F and T_{pk}, the relative differences will only be large for smaller values of F. Hence, the effects of alpha ejection on He fractional losses will only be significant for very low-temperature thermal events in nature, and effects on laboratory-

1140 measured He release patterns would be most pronounced for low-temperature heating steps. See
1141 text for further discussion.
1142
1143 **Figure 11.** Comparison of He diffusion in natural monazite, apatite, zircon, titanite and rutile.
1144 Sources for data: monazite – this study; apatite and zircon – Cherniak et al. (2009); rutile and
1145 titanite – Cherniak and Watson (2011). He diffusion in monazite is slightly slower than He
1146 diffusion in zircon normal to c, and falls roughly between diffusion along [100] and [001] in
1147 rutile. Helium diffusion in titanite, and rutile along [001] are comparable, while He diffusion in
1148 titanite is intermediate between diffusion in zircon normal and parallel to c. He diffusion in
1149 apatite is about five orders of magnitude faster than in monazite. Among this group of accessory
1150 minerals, activation energies for He diffusion in monazite, titanite and zircon are similar (~150
1151 kJ/mol) while those for apatite and rutile are somewhat lower (~120 kJ/mol).
1152
1153 **Figure 12.** Fraction of He remaining during isothermal heating at 250°C as a function of time
1154 from grains of apatite, titanite, zircon, monazite and rutile. Curves are plotted using the diffusion
1155 parameters from Cherniak et al. (2009) for zircon and apatite, Cherniak and Watson (2011) for
1156 rutile and titanite and this study for monazite. Spherical geometry (with grain radii of 50 μm for
1157 monazite and titanite, 200 μm radii for apatite) and the analytical expression for fraction of
1158 diffusant lost from a sphere (Crank, 1975) are used for apatite, monazite and titanite since no
1159 anisotropy is observed, while cylindrical geometry (with grain radii of 50 μm and lengths of 100
1160 μm) and the CYLMOD code (Watson et al., 2010) are used to calculate fractional He loss for
1161 rutile and zircon given their anisotropy of diffusion. For grains of roughly equivalent size,

monazite should be most retentive of He, followed by rutile, zircon and titanite. Apatite is the least retentive of He among these accessory mineral phases. See text for additional discussion.

Figure 1

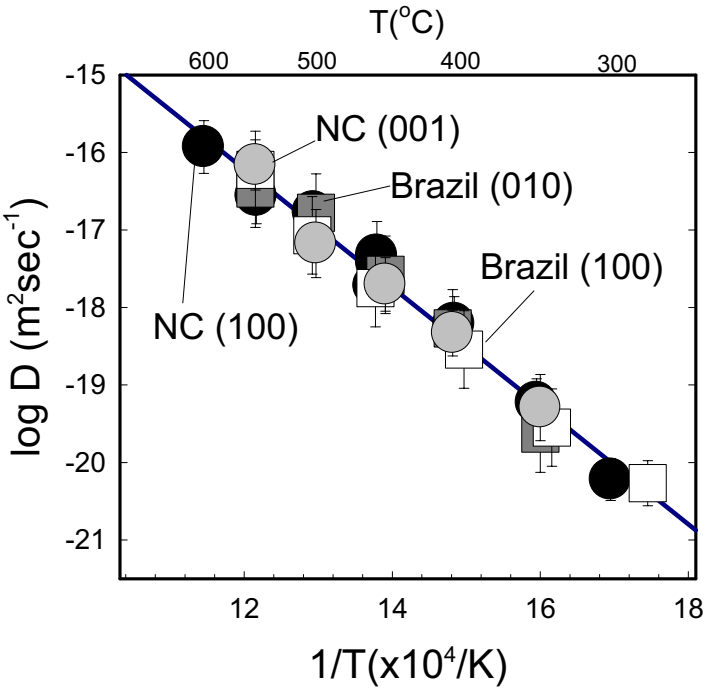

Figure 2

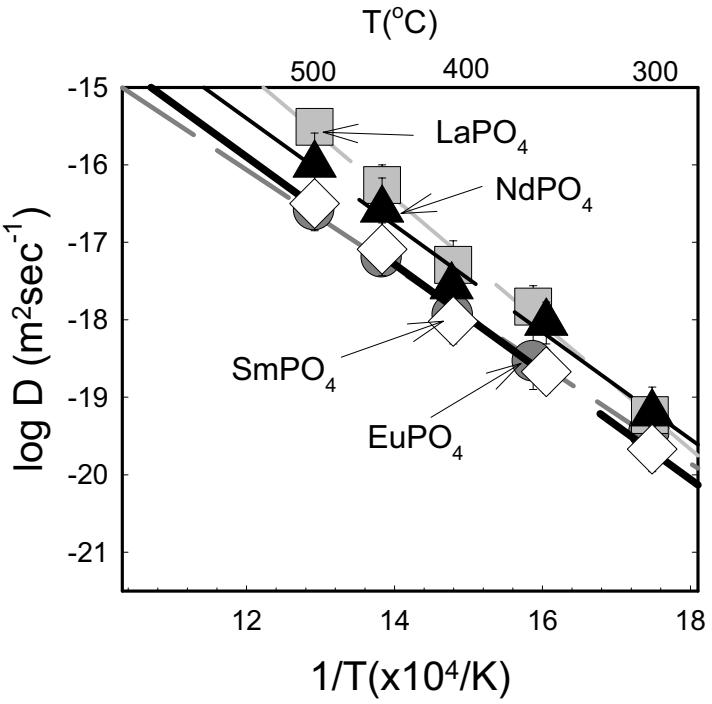

This is a preprint, the final version is subject to change, of the American Mineralogist (MSA)
Cite as Authors (Year) Title. American Mineralogist, in press.
(DOI will not work until issue is live.) DOI: http://dx.doi.org/10.2138/am.2014.4353

Figure 3

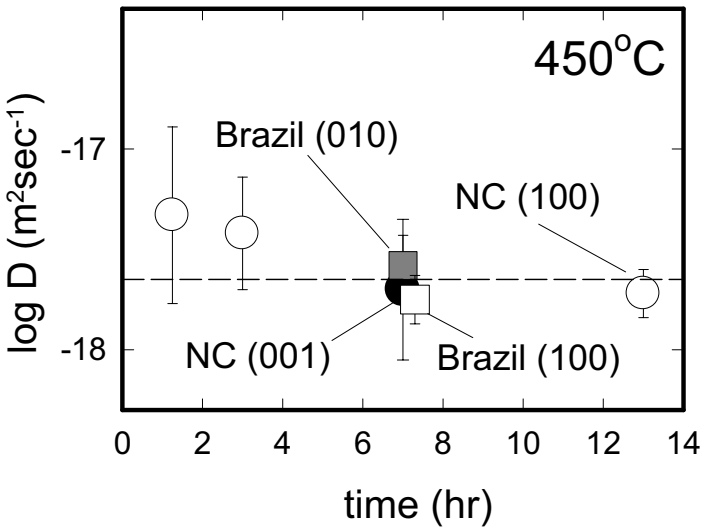

This is a preprint, the final version is subject to change, of the American Mineralogist (MSA)
Cite as Authors (Year) Title. American Mineralogist, in press.
(DOI will not work until issue is live.) DOI: http://dx.doi.org/10.2138/am.2014.4353

Figure 4a

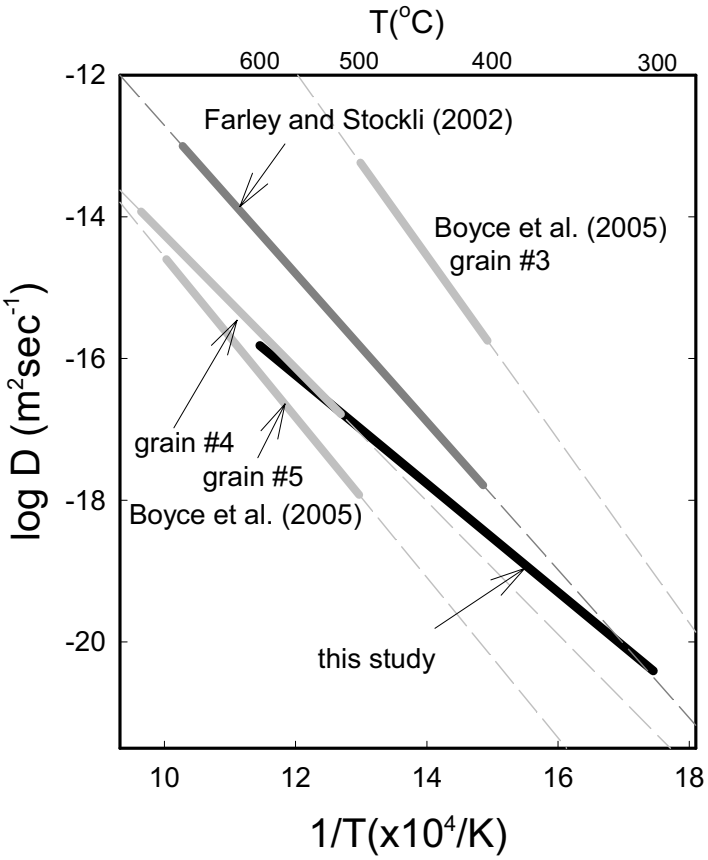

Figure 4b

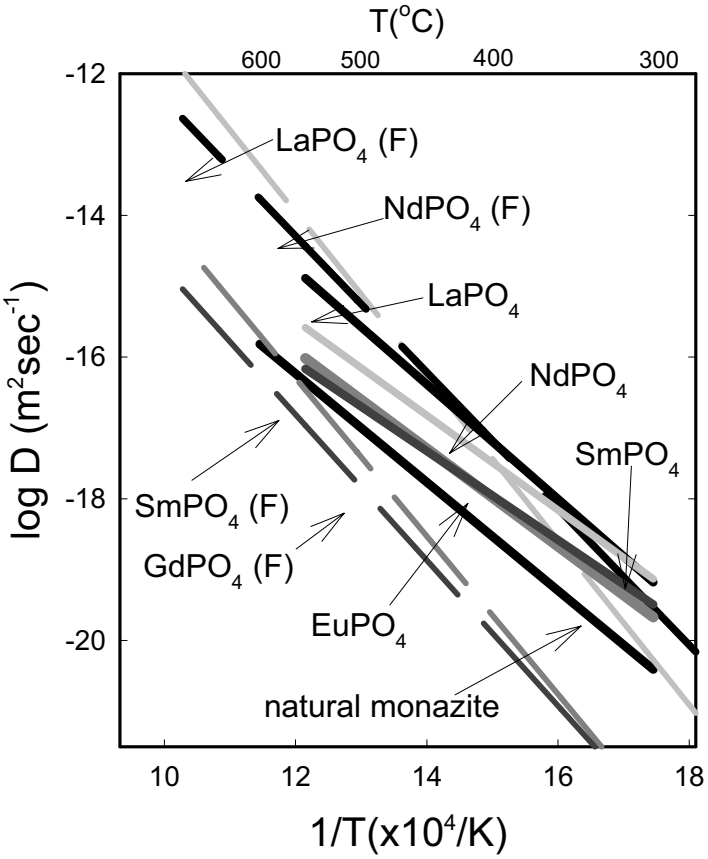

Figure 5a

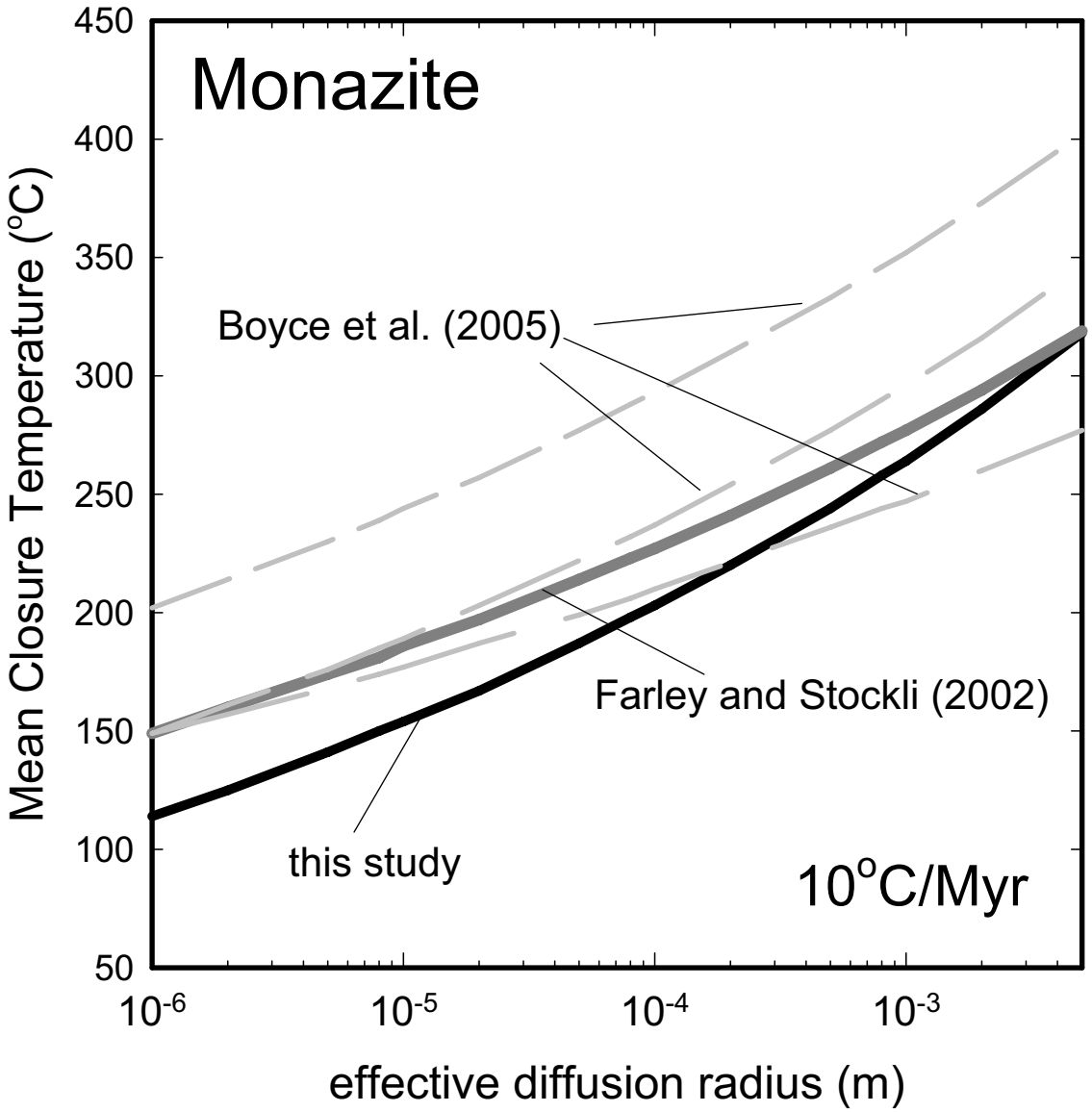

Figure 5b

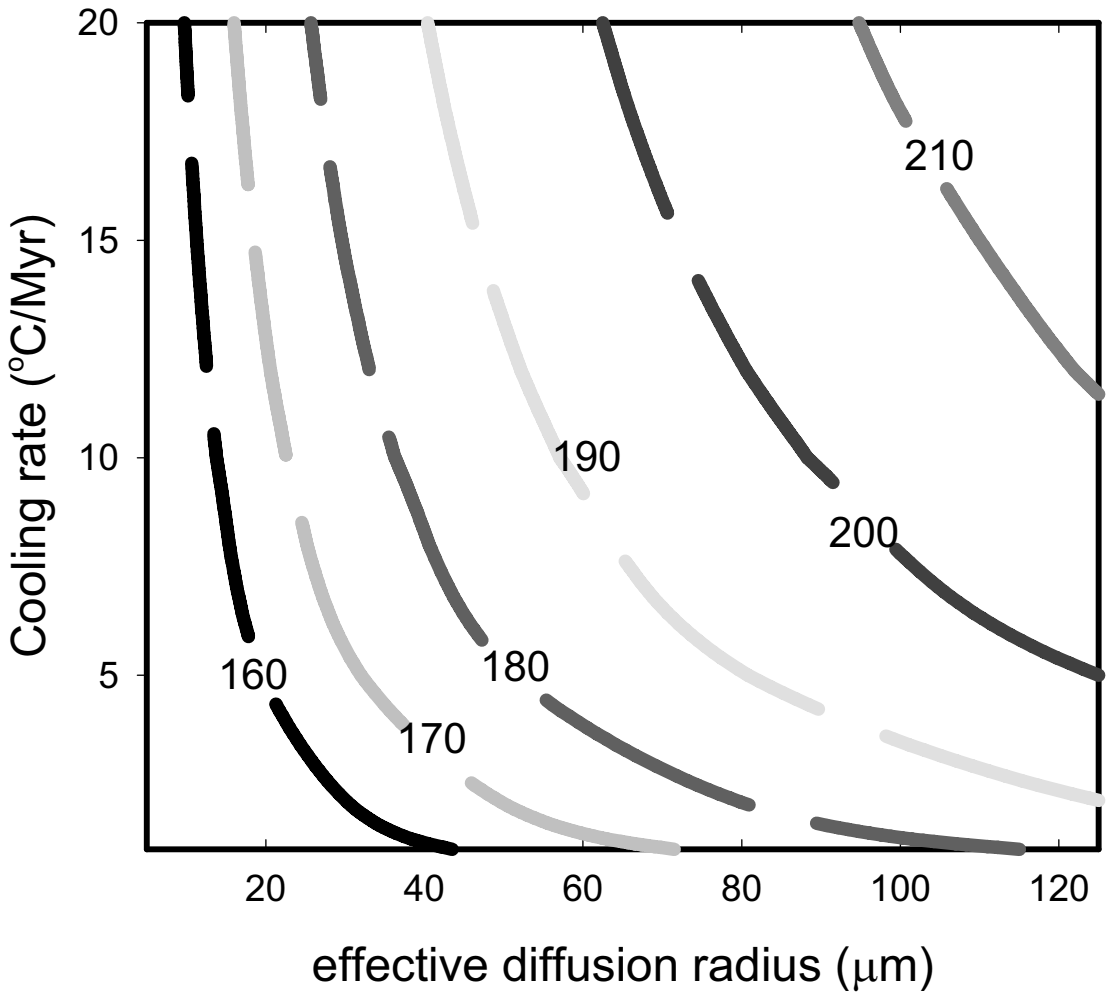

This is a preprint, the final version is subject to change, of the American Mineralogist (MSA)
Cite as Authors (Year) Title. American Mineralogist, in press.
(DOI will not work until issue is live.) DOI: http://dx.doi.org/10.2138/am.2014.4353

Figure 6

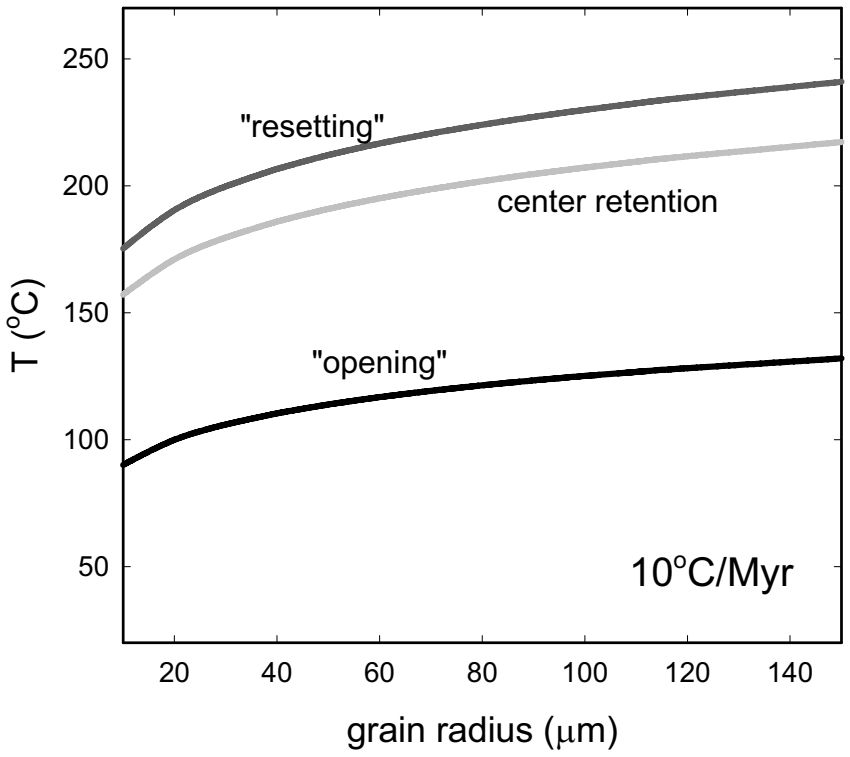

Figure 7.

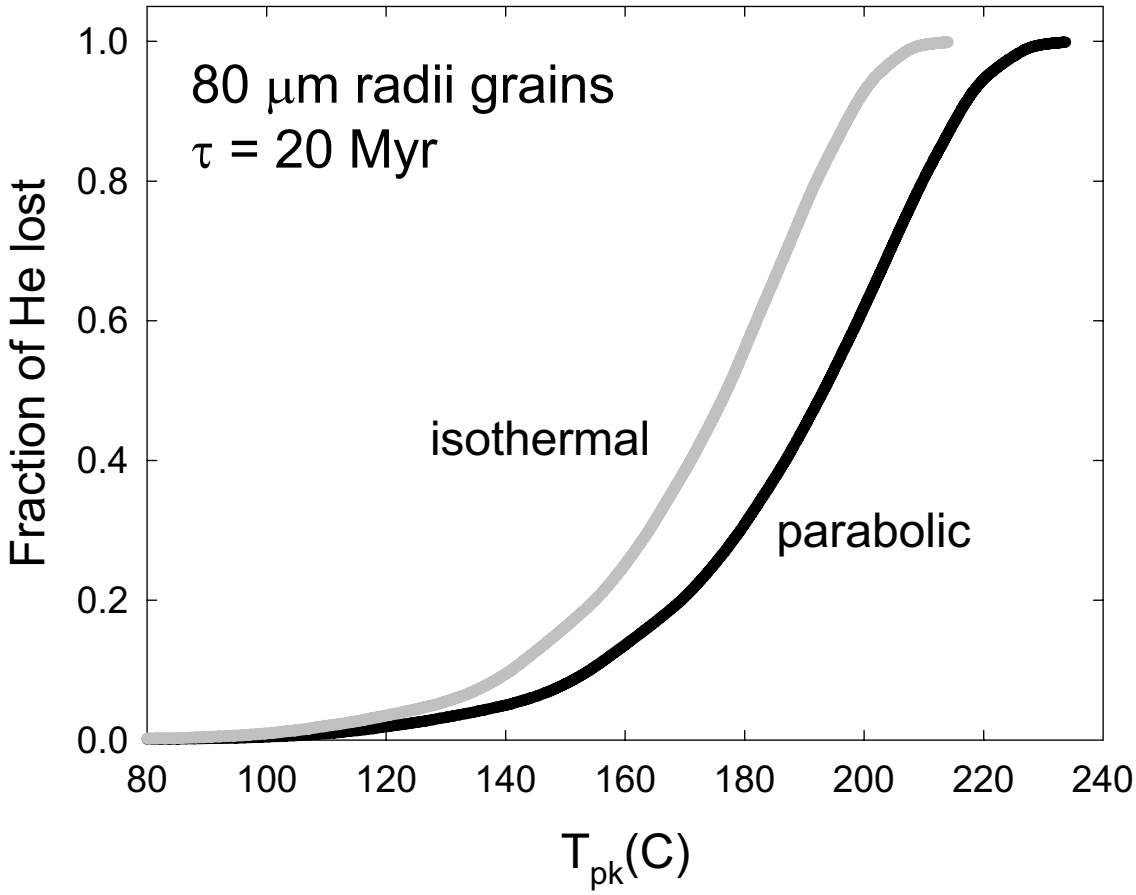

Figure 8

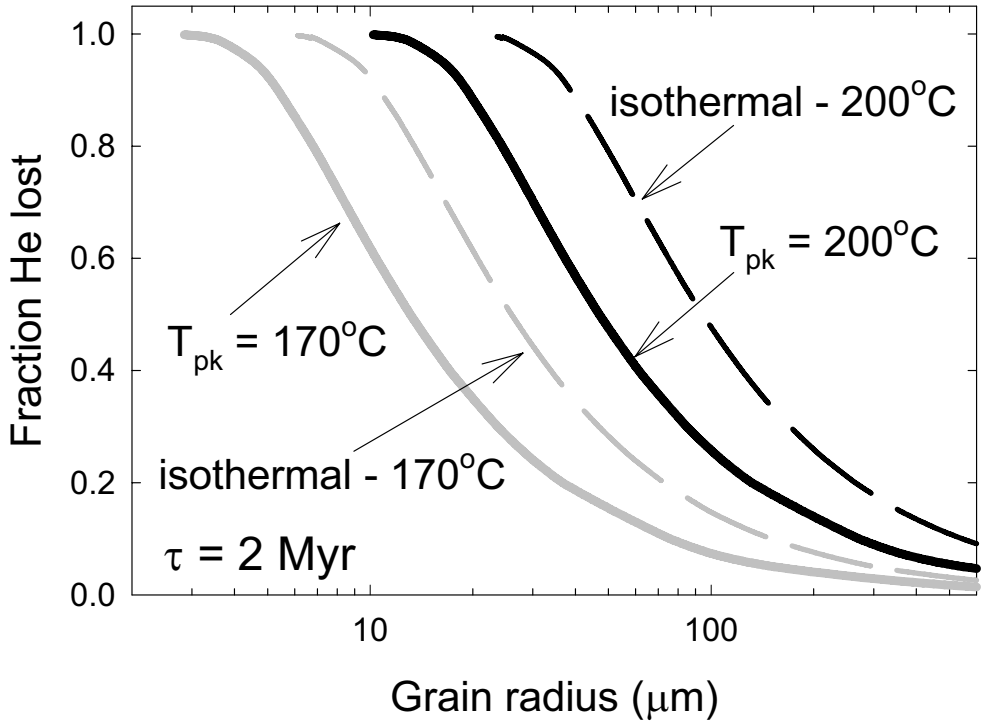

This is a preprint, the final version is subject to change, of the American Mineralogist (MSA)
Cite as Authors (Year) Title. American Mineralogist, in press.
(DOI will not work until issue is live.) DOI: http://dx.doi.org/10.2138/am.2014.4353

Figure 9

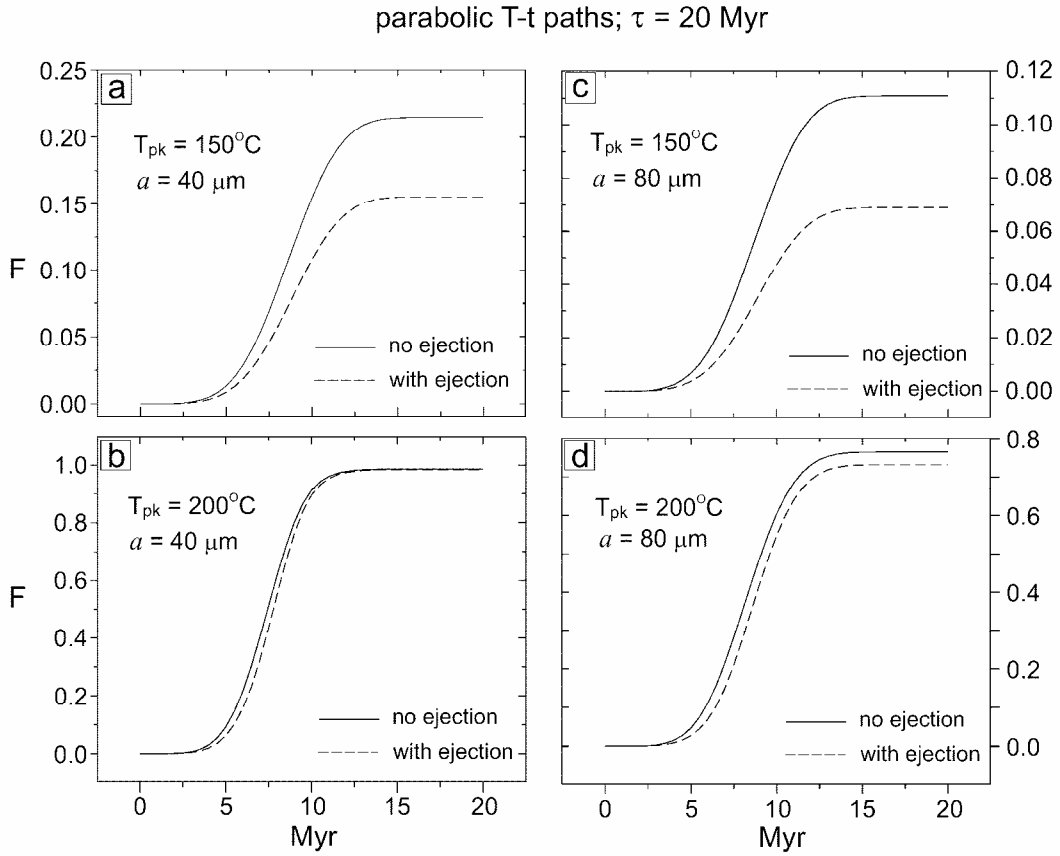

This is a preprint, the final version is subject to change, of the American Mineralogist (MSA)
Cite as Authors (Year) Title. American Mineralogist, in press.
(DOI will not work until issue is live.) DOI: http://dx.doi.org/10.2138/am.2014.4353

Figure 10

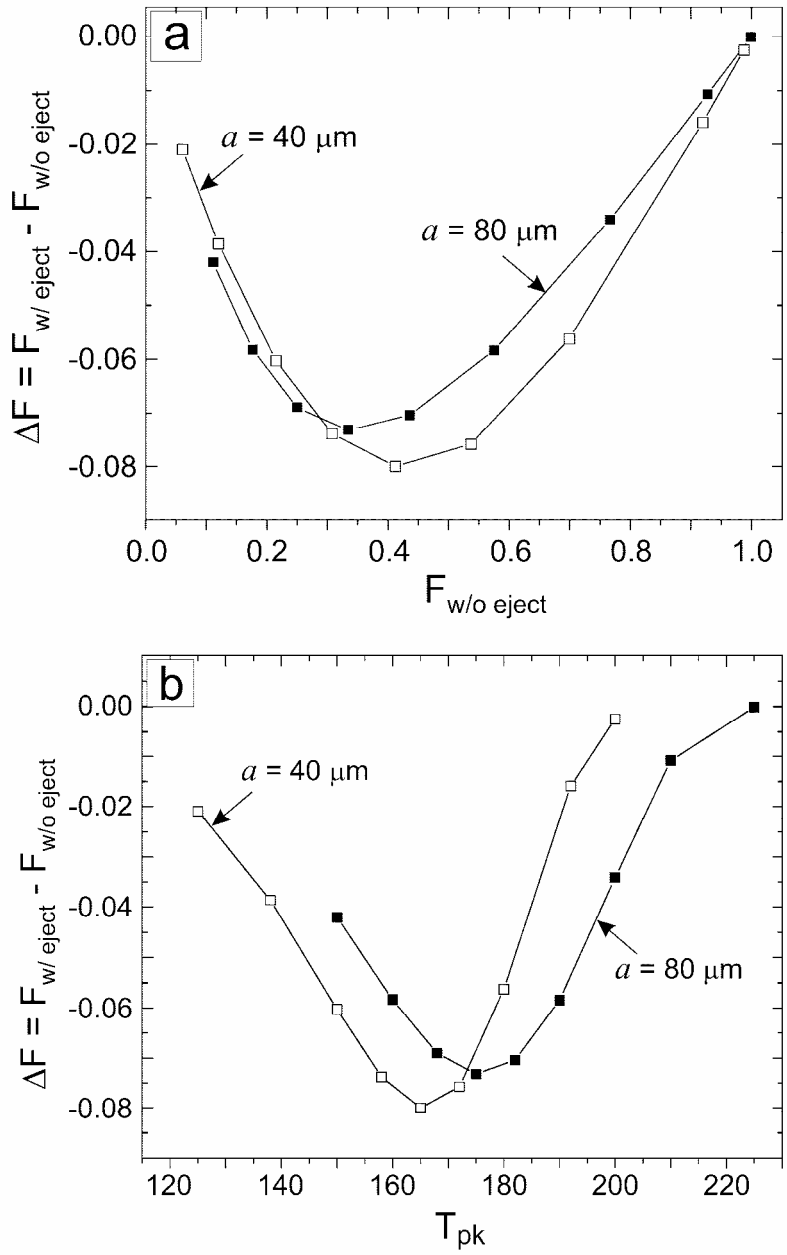

Figure 11

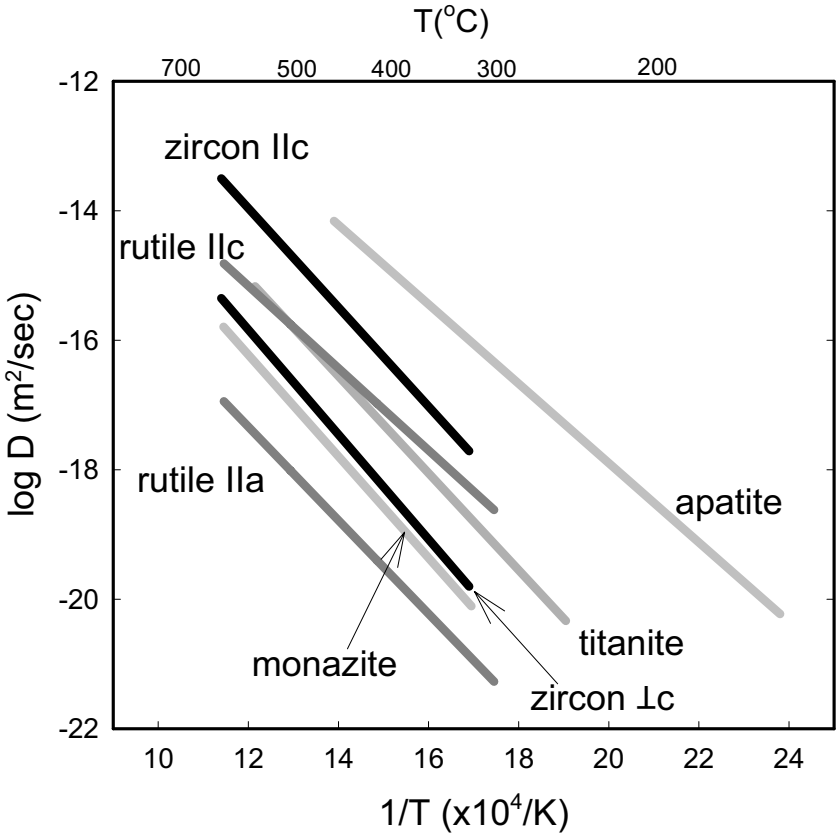

Figure 12